
















RESEARCH ARTICLE | JUNE 16 2022

CHES: The future direct geometry spectrometer at the second target station


Special Collection: [New Science Opportunities at the Spallation Neutron Source Second Target Station](#)

G. Sala ; M. Mourigal ; C. Boone ; N. P. Butch ; A. D. Christianson; O. Delaire ;
A. J. DeSantis ; C. L. Hart ; R. P. Hermann ; T. Huegle ; D. N. Kent; J. Y. Y. Lin ; M. D. Lumsden ;
M. E. Manley ; D. G. Quirinale ; M. B. Stone ; Y. Z 




Rev. Sci. Instrum. 93, 065109 (2022)

<https://doi.org/10.1063/5.0089740>



APL Machine Learning
2023 Papers with Best Practices in Data Sharing and Comprehensive Background
[Read Now](#)



CHES: The future direct geometry spectrometer at the second target station

Cite as: *Rev. Sci. Instrum.* **93**, 065109 (2022); doi: [10.1063/5.0089740](https://doi.org/10.1063/5.0089740)

Submitted: 28 February 2022 • Accepted: 25 May 2022 •

Published Online: 16 June 2022



View Online



Export Citation



CrossMark

G. Sala,^{1,a)} M. Mourigal,² C. Boone,¹ N. P. Butch,^{3,4} A. D. Christianson,⁵ O. Delaire,⁶
A. J. DeSantis,¹ C. L. Hart,¹ R. P. Hermann,⁵ T. Huegle,⁷ D. N. Kent,¹ J. Y. Y. Lin,¹ M. D. Lumsden,⁸
M. E. Manley,⁵ D. G. Quirinale,⁸ M. B. Stone,⁸ and Y. Z.^{9,10,11}

AFFILIATIONS

¹Spallation Neutron Source, Second Target Station, Oak Ridge National Laboratory, Oak Ridge, Tennessee 37831, USA

²School of Physics, Georgia Institute of Technology, Atlanta, Georgia 30332, USA

³NIST Center for Neutron Research, National Institute of Standards and Technology, Gaithersburg, Maryland 20899, USA

⁴Maryland Quantum Materials Center, Department of Physics, University of Maryland, College Park, Maryland 20742-4111, USA

⁵Materials Science and Technology Division, Oak Ridge National Laboratory, Oak Ridge, Tennessee 37831, USA

⁶Department of Physics, Duke University, Durham, North Carolina 27708, USA

⁷Neutron Technology Division, Oak Ridge National Laboratory, Oak Ridge, Tennessee 37831, USA

⁸Neutron Scattering Division, Oak Ridge National Laboratory, Oak Ridge, Tennessee 37831, USA

⁹Department of Nuclear, Plasma, and Radiological Engineering, University of Illinois at Urbana-Champaign, Urbana, Illinois 61801, USA

¹⁰Department of Electrical and Computer Engineering, University of Illinois at Urbana-Champaign, Urbana, Illinois 61801, USA

¹¹Beckman Institute for Advanced Science and Technology, University of Illinois at Urbana-Champaign, Urbana, Illinois 61801, USA

Note: Paper published as part of the Special Topic on New Science Opportunities at the Spallation Neutron Source Second Target Station.

^{a)} Author to whom correspondence should be addressed: salag@ornl.gov

ABSTRACT

CHES, chopper spectrometer examining small samples, is a planned direct geometry neutron chopper spectrometer designed to detect and analyze weak signals intrinsic to small cross sections (e.g., small mass, small magnetic moments, or neutron absorbing materials) in powders, liquids, and crystals. CHES is optimized to enable transformative investigations of quantum materials, spin liquids, thermoelectrics, battery materials, and liquids. The broad dynamic range of the instrument is also well suited to study relaxation processes and excitations in soft and biological matter. The 15 Hz repetition rate of the Second Target Station at the Spallation Neutron Source enables the use of multiple incident energies within a single source pulse, greatly expanding the information gained in a single measurement. Furthermore, the high flux grants an enhanced capability for polarization analysis. This enables the separation of nuclear from magnetic scattering or coherent from incoherent scattering in hydrogenous materials over a large range of energy and momentum transfer. This paper presents optimizations and technical solutions to address the key requirements envisioned in the science case and the anticipated uses of this instrument.

© 2022 Author(s). All article content, except where otherwise noted, is licensed under a Creative Commons Attribution (CC BY) license (<http://creativecommons.org/licenses/by/4.0/>). <https://doi.org/10.1063/5.0089740>

I. INTRODUCTION

Inelastic neutron scattering (INS) is a powerful experimental technique to study the dynamical properties of materials as a

function of temperature, electric field, magnetic field, and pressure. This technique takes advantage of several fundamental properties of neutrons. The wavelength of moderated neutrons is well

matched to interatomic distances in many materials; neutron energies are comparable to characteristic energies of atomic motions in many materials; neutrons have a magnetic moment allowing the study of magnetic fluctuations and structures; and the neutron weakly interacts with matter allowing it to penetrate through complex sample environments. Furthermore, the scattering function $S(Q, \omega)$ derived from neutron scattering measurements is proportional to the imaginary part of a generalized momentum and energy-dependent susceptibility, which makes a quantitative comparison between experiment and theory straightforward. Transformative advances in our understanding of materials for energy, quantum information, health, and environmental applications require knowledge of the complex physics underlying their dynamical properties. In condensed matter and biology, new materials are often available in limited quantities, particularly as single crystals, which often lead to long experiments and impede progress. Furthermore, spectrometers need to be designed to host complicated sample environments, such as high field magnets and pressure cells, which pose challenges due to their intrinsic high background. Thus, increasing measurement sensitivity to enable studies on smaller samples is considered one of the highest priorities for the design of a new inelastic spectrometer at the Second Target Station (STS) of the Spallation Neutron Source (SNS) at Oak Ridge National Laboratory (ORNL).

The CHESSE spectrometer is designed to overcome these issues by trading high flux (HF) for resolution to meet the requirements of diverse experiments. The broad wavelength band employed by this instrument naturally lends itself to performing survey-type experiments and to study materials where dynamic processes exist over a wide energy and momentum range. The high flux and the possibility of using Repetition Rate Multiplication (RRM)^{1–4} will increase the quality of the dataset and decrease the data collection times. Furthermore, the possibility to employ polarization analysis⁵ will enrich the level of information acquired during the measurement, allowing the disentanglement of coherent from incoherent signals and magnetic from structural features, as well as the ability to better characterize anisotropic magnetization distribution in crystals. CHESSE is expected to impact a broad scientific user community spanning quantum and magnetic materials,^{6–14} superconductors,^{15–17} thermoelectric materials,^{18–21} energy and battery materials,^{22–26} life sciences,^{27–34} liquids and complex fluids,^{35–41} and soft matter.^{42–46} CHESSE is poised to build upon these established user communities while simultaneously broadening the scope of problems that can be solved by cold neutron spectroscopy. This additional component to the CHESSE user community will come from individuals who considered neutron spectroscopy prohibitive due to sample size requirements, and it will most likely be composed of groups that work at the forefront of developing new materials, where large single crystals are typically not available.

This manuscript is organized as follows: After a brief summary of the expected performance and engineering layout, we show the latest developments in guide, chopper, and detector optimizations. We then conclude by showing some experiment simulations to demonstrate the capabilities of CHESSE.

II. INSTRUMENT PERFORMANCE REQUIREMENTS

CHESSE is designed as a cold neutron high flux chopper spectrometer with a medium-coarse elastic energy resolution of

$2\% \leq \delta E/E \leq 5\%$. An energy resolution coarser than $\delta E/E > 5\%$ is less useful for cold neutron experiments because the elastic line quickly overshadows the features at low energy transfer that are one of the primary interest for the CHESSE science case.

A direct-geometry spectrometer optimized for the cold neutron energy range usually employs a pair of high-speed choppers that defines the incident energy, E_i , and the energy resolution δE . We will refer to these choppers as P- (“pulse-shaping”) and M- (“monochromator”) choppers. The energy resolution contains three terms added in quadrature that derive from the source pulse width Δt_S , the M-chopper burst time Δt_M , and the time-of-flight uncertainty in the secondary spectrometer Δt_D , determined by the detector pixel and sample sizes. Our simulations show that the P-chopper mainly controls the resolution profile (by suppressing the so-called Ikeda tail⁴⁷) and the overall flux. At the elastic line, the energy resolution can be well approximated by the following equation:^{48–50}

$$(\delta E)^2 = \frac{m_n^2 v^6}{L_1^2} \left(1 + \frac{L_2}{L_3}\right)^2 (\Delta t_S)^2 + \frac{m_n^2 v^6}{L_1^2} \left(1 + \frac{L_1 + L_2}{L_3}\right)^2 (\Delta t_M)^2 + \frac{m_n^2 v^6}{L_3^2} (\Delta t_D)^2, \quad (1)$$

where m_n is the neutron mass, v is its speed, L_1 is the distance from the source to the M-chopper, L_2 is the distance from the M-chopper to the sample, and L_3 is the distance from the sample to the detector as shown in Fig. 1.

Our goal is to measure inelastic or quasi-elastic neutron scattering (QENS) arising from small samples. Thus, we must be able to tighten the energy resolution without losing too much intensity. As described by Ehlers *et al.*,⁵⁰ the best trade-off between energy and resolution is accomplished by matching the three contributions to the resolution in Eq. (1),

$$\frac{L_2 + L_3}{L_1 L_3} v \Delta t_S = \frac{L_1 + L_2 + L_3}{L_1 L_3} v \Delta t_M = \frac{v \Delta t_D}{L_3}. \quad (2)$$

These relations can be used to derive boundary conditions for the three major lengths (L_i) during the spectrometer design.

The tube moderator was designed and optimized for time integrated brightness,⁵¹ which corresponds to the integral of the pulse emission-time distribution at the selected wavelength over the emission time, times the repetition rate of the source, and it is predicted to deliver a pulse width that can be expressed as $v \Delta t_S \approx 0.23$ m in the wavelength range $\lambda_i \approx 2–20$ Å. Thus, the contribution of the source to the energy resolution becomes

$$\frac{\delta E_S}{E} = 2 \frac{L_2 + L_3}{L_1 L_3} v \Delta t_S \leq \frac{0.05}{\sqrt{3}}, \quad (3)$$

where $E = m_n v^2/2$. Our optimizations using Eqs. (1)–(3) result in $L_1 = 30$ m, $L_2 = 1.5$ m, and $L_3 = 2.5$ m that provide a resolution of $\delta E/E = 5\%$ at the peak of the tube moderator spectrum, $\lambda = 3$ Å. A comparison of the simulated energy resolution at the elastic line for CHESSE, vs current worldwide leading chopper spectrometers is shown in Fig. 2.

The simulations for the CHESSE energy resolution curves shown in Fig. 2 used purely monochromatic beams (no RRM included) for two possible configurations of the M-chopper that represent

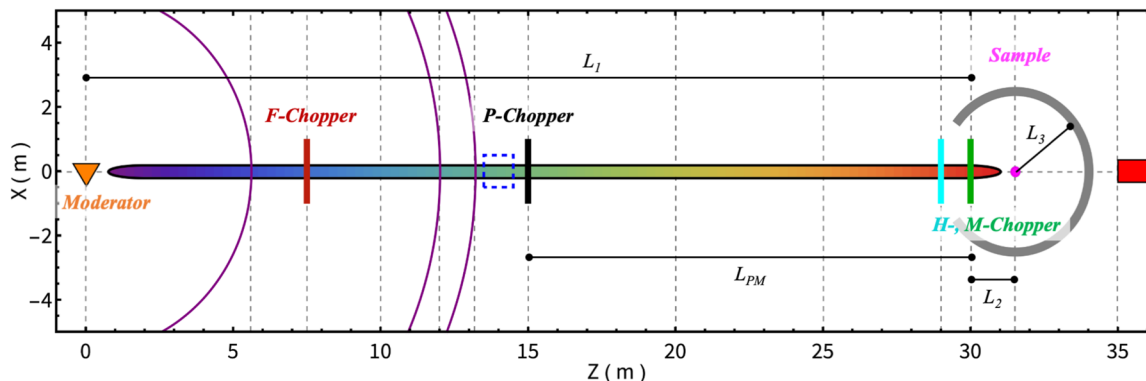


FIG. 1. Diagram of the CHES beamline. The diagram of the CHES beamline is showing the location of the main components: tube moderator, choppers, operations shutter (blue dashed box), sample, and detectors. We also highlight the three lengths of the instruments, L_i , which determine the elastic energy resolution shown in Eq. (1).

a High Flux (HF) and a High Resolution (HR) mode of operation. The HF mode was simulated using an 8° opening of the M-chopper, whereas the HR mode used a 6° opening. Simulations were done employing McStas⁵⁵ and MCViNE.^{56,57} A cylindrical vanadium sample with the same characteristics ($\varnothing = 6.1$ mm, 50 mm tall) as the standard calibration sample used at the Cold Neutron Chopper Spectrometer (CNCS)⁵² was created for the scattering kernel. We performed a series of simulations using the same incident energies as the experimental dataset collected at CNCS in 2018. Our simulated data were reduced and analyzed using Mantid⁵⁸ to extract the profile at the elastic line. Finally, this profile was fit with a Gaussian function and the full width at half maximum (FWHM) was used

for the comparisons in Fig. 2. Equivalent datasets measured at LET⁵³ and AMATERAS⁵⁴ were retrieved from their respective websites with agreement of the respective instrument scientists. CHES wavelength dependent energy resolution is in good agreement with the Ikeda–Carpenter resolution function in Eq. (1), shown as a dashed black line in Fig. 2. The energy resolution of the CHES HF configuration is similar to the CNCS HF configuration (green curve). The LET (blue curve) and AMATERAS (purple curve) instruments have better energy resolution in their standard mode of operation when compared to the CHES HF mode. However, the CHES HR mode provides similar resolution. The chopper configuration proposed for CHES allows for flexibility in operation trading energy resolution for flux during measurements.

Due to the rather compact length of CHES, the resulting bandwidth (i.e., the difference between the longest and shortest incident wavelengths available for use) at a $f_s = 15$ Hz source frequency will effectively be $\sim 7\text{--}8$ Å wide in the first frame. This wide bandwidth, which naturally favors the use of the RRM mode, will be very beneficial for the study of materials where the intrinsic energy scales are widespread or unknown. The CHES key performance parameters are presented in Table I.

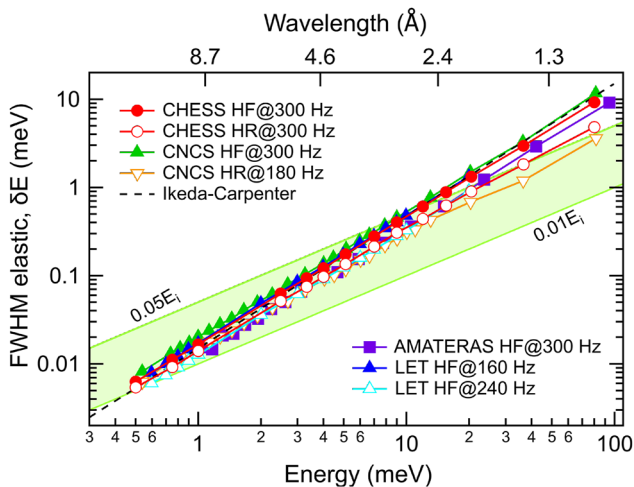


FIG. 2. Energy resolution (δE) at the elastic line. The comparison of the CHES simulated energy resolution for a monochromatic beam for two configurations High Flux (HF) and High Resolution (HR), further described in the text, shows an excellent agreement with our expectations, matching the data collected at CNCS⁵² in HF, LET⁵³ and AMATERAS⁵⁴ in HR mode. The green band corresponds to the resolution range $1\% \leq \delta E/E \leq 5\%$.

TABLE I. CHES key performance parameters.

Parameter	Description
Beam size at sample	Round, $1 \leq \varnothing \leq 22$ mm
Detector coverage	$\Omega = 2\pi$ sr
Incident energy range	$0.2 \leq E_i \leq 80$ meV
Incident wavelength range	$1 \leq \lambda_i \leq 20$ Å
Elastic energy resolution (δE)	$2\% \leq \delta E/E \leq 5\%$
Total bandwidth ($\Delta\lambda$)	7–8 Å
Q-range	$0.025 \leq Q \leq 10$ Å ⁻¹
Q-resolution	$0.02 \leq \Delta Q/Q \leq 0.05$
Polarization	XYZ polarization analysis
Beam divergence at sample	FWHM = 2°

TABLE II. CHES chopper specifications. The symbol * is used to denote double-disk choppers, and the symbol † for horizontal-axis choppers. z represents the distance from the tube moderator.

Name	z : (m)	Disk: (m)	Apertures	f : (Hz)
F-chopper*	7.5	$\text{Ø} = 1.24$	1	15
P-chopper*	15.0	$\text{Ø} = 0.6$	2	300
T_0 -chopper†	18.5	$\text{Ø} = 1.24$	N/A	15
H-chopper*	29.3(3)	$\text{Ø} = 0.7$	9–10	15
M-chopper*	30.0	$\text{Ø} = 0.6$	1	300

III. ENGINEERING OUTLINE

Due to space constraints, the current layout of the CHES instrument is shown in Figs. 13 and 14. CHES has a total flight-path of 34 m from moderator to detectors. The two fast ($f \geq 300$ Hz) double disk choppers: P-chopper and M-chopper are located at the pinch points of the guide system at $L_P = 15$ and $L_M = 30$ m, respectively. The frame-overlap (F-chopper), T-zero (T_0),⁵⁹ and hand (H-chopper) choppers are placed at $L_F = 7.5$, $L_{T_0} = 18.5$, and $L_H = 29.3$ m, respectively. Table II summarizes the chopper characteristics whose respective roles are discussed further in the text.

The backend of the instrument has been designed as a three floor building, housing: a utility room for the detector vacuum system and control racks on the first floor, the instrument control center and a sample preparation laboratory for non-irradiated materials on the second floor, and the sample environment storage area with direct access to the instrument on the third floor. An elevator to transport materials and equipment will serve all three floors, while a bridge and a staircase will allow users and personnel to move across the floors and onto the STS mezzanine.

A. Detector vacuum vessel

Following successful instruments such as SEQUOIA,⁶⁰ ARCS,⁶¹ LET,⁶² and AMATERAS,⁶³ CHES will have its detectors in high vacuum ($\leq 10^{-8}$ mbar) to reduce the background due to air-scattering. The current design, shown in Fig. 3, uses flange mounts to secure sample environments to the instrument, sealing the detector tank before pulling vacuum. The sample pit has a diameter of 1.5 m and can host large sample environments including those with ancillary equipment attached, such as collimators or ^3He analyzers. This solution is similar to that used on ARCS and SEQUOIA.⁶⁴ However, there will not be a gate valve that physically separates the sample space from the detector space.

The vessel itself is cylindrical, 7.3 m tall including the ribbing skeleton with a diameter of 6.8 m. The total volume is 200 m³. An airtight hatch at the back will grant access to the detector tank and seal the structure. A stainless-steel (SS) ribbing skeleton surrounds the vacuum vessel and provides structural support. Vacuum ports are positioned between the ribbing around the vessel and the intra spaces can also be used to place trenches for pipes and cables. Borated polyethylene will be placed around the outside of the vacuum vessel, and ZHIP⁶⁵ mix panels will be used inside for neutronic shielding. Additional biological shielding will

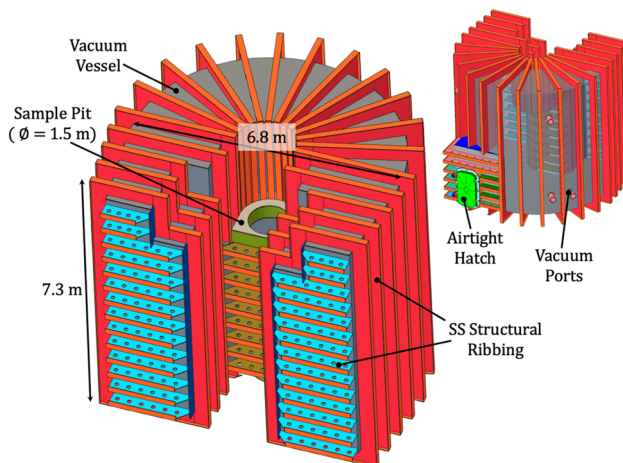


FIG. 3. CHES vacuum vessel layout. The vessel itself is cylindrical, 7.3 m tall including the ribbing skeleton with a diameter of 6.8 m. The sample pit, $\text{Ø} = 1.5$ m, is designed to host large sample environments with ancillary equipment. An airtight hatch grants access to the detector tank and seals it. Vacuum ports and trenches for pipes and cables are embedded in the stainless steel ribbing. Radiation shields will be integrated in the design of the structure after neutronics analysis.

be placed on the outside of the vessel to maintain a radiation level of ≤ 0.25 mrem/h.

B. Sample environment

CHES will have a dedicated bridge crane at the beamline to move heavy sample environment equipment around the third floor and secure them to the flange mount. Details about sample environment and polarization devices will be provided in following publications. CHES is designed to be compatible with the following sample environments:

- A bottom loading Closed-Cycle Refrigerator (CCR), $5 \leq T \leq 800$ K, with the potential for powder sample changers over a narrower temperature range.
- An orange cryostat (liquid Helium cryostat), $1.7 \leq T \leq 323$ K, with the possibility to couple a ^3He or dilution refrigerator inserts.
- A ^3He insert, $0.3 \leq T \leq 10$ K.
- A dilution refrigerator insert, $20 \text{ mK} \leq T \leq 1$ K.
- A compensated vertical field cryo-magnet, $H > 8$ T, $1.7 \leq T \leq 400$ K, with the possibility to couple an ^3He or dilution refrigerator inserts.
- A non-compensated vertical field cryo-magnet, $H_{\text{max}} \approx 18$ T, $1.7 \leq T \leq 400$ K, with the possibility to couple a ^3He or dilution refrigerator inserts.
- A horizontal field 5 T magnet.
- A furnace with a niobium or vanadium shield and with option for quartz gas flow insert, $300 \leq T \leq 1900$ K.
- A high temperature neutron electrostatic levitator⁶⁶ (NESL), $300 \leq T \leq 3000$ K.

Auxiliary systems, such as pressure cells, or laser illumination are currently being evaluated.

IV. NEUTRON OPTICS

In order to fully utilize the high brightness of the STS tube moderator, the CHES neutron optics (i.e., guide, choppers, collimators, and slits) have been re-optimized from the original concept paper.⁶⁷ In this section, we first make a detailed comparison between traditional square cross section guides vs the new octagonal guides, and then we discuss choppers and radial collimators.

A. Comparison of the octagonal and square guide systems

Neutron transport from the moderator to the sample has always been one of the biggest challenges during the design and optimization phase of a neutron scattering instrument. This is primarily due to the large number of parameters involved in the analysis. Quantities, such as resolution and flux, are the standard figure of merit (FoM) to describe the performance of the instrument, but they are insufficient to provide a full optimization. A brilliance transfer (BT) calculation is more suited to study the neutron beam phase space, but the analytical approximations can be misleading, especially when shapes more complex than rectangular, straight guides are considered.

The original CHES guide system leveraged the optical property of an ellipse (or ellipsoid in three dimensions) that a neutron passing through one of the ellipse focal points is naturally reflected toward the other. Building a guide system having a perfect ellipsoidal shape is not feasible with current technology, but we can approximate this shape with an octagonal cross section guide that mimics the basic property of the ellipsoid (see Fig. 11). The overall shape of the guide can be thought of an array of super-mirrors, coated with layers of Ni/Ti representing specific m -values,⁶⁸ that reflect any incident neutron toward one of the focal points where, for example, a chopper or the sample is located. However, it has been shown that placing the focal point behind the moderator leads to a better guide gain for a broader range of wavelengths.⁶⁹

We highlight that the elliptic geometry has been already extensively studied, especially with regards to the neutron transport in very long instruments ($L \geq 100$ m) for the European Spallation Source (ESS).⁷⁰ These studies confirmed that an elliptic geometry is superior to a common straight guide, especially to transport thermal neutrons, and we now report the main conclusions of these analyses.

Previous investigations of guides included four shapes: elliptic, parabolic, ballistic, and straight.⁷⁰ The primary findings are that the elliptic and parabolic geometries perform almost equally well and are considerably superior to the other two geometries, except for low-divergence, cold neutrons, where the performances were found to be similar. In addition, the authors observed that it was possible to transport thermal neutrons more than 100 m using elliptic guides with only a 10% loss in the phase space density for divergences up to $\pm 0.5^\circ$.

Despite the benefits of elliptic or parabolic guides for neutron transport, these geometries are affected by aberrations (e.g., “coma”) that need to be taken into account during design. For our initial refinement of the CHES guide system, we refer to the analysis done by Bentley *et al.*,⁷¹ which represents an excellent first step toward the understanding/correction of optical aberrations in elliptic neutron guides. In short, the authors show that coma aberration results from extended sources where the off-axis rays have a different focal

length from on-axis rays, leading to multiple reflections in the guide system. This also produces uneven distributions in the neutron beam divergence, which complicates the resolution function. To solve these problems, the authors proposed a hybrid elliptic–parabolic guide geometry. Using this new kind of neutron guide shape, it is possible to condition the neutron beam and remove almost all aberrations, while providing comparable performances in beam flux as a standard elliptic neutron guide.

Furthermore, in our guide design, we need to consider hosting a T_0 -chopper or a curved section that removes the direct line of sight to the source like at CNCS and AMATERAS. The latter choice may present an incompatibility with the elliptic shape of our guides and, as such, was disregarded. A recent study⁷² argues that it is also possible to integrate a kinked double-elliptic solution for neutron transport from a small source to a small sample. This guide system consists of two elliptical parts connected by a linear kinked section, and it is shown to deliver a high brilliance transfer as well as a homogeneous divergence distribution while avoiding the direct line of sight of the source.

Our results also showed that the best neutron transport is achieved using a hybrid guide profile, consisting of two ellipses with different semi-major axes that meet exactly at the mid-point. This profile was benchmarked using a combination of polynomial functions, hyperbolic tangents, and parabolas. The final optimizations for these three curves were akin to ellipsoid shapes, consistent with Refs. 71 and 72, which were then selected as final functions for the guide profile optimization (see Appendix A for more details).

Finally, we also considered guide illumination in the CHES design. Traditional moderators are rectangular in shape, which tends to favor a rectangular/square guide cross section. However, the CHES tube moderator has a circular surface, and a square guide cross section may result in an under(over) illumination of the guides, depending on the relative size of the source and guide entrance. Based upon these noted considerations, we chose to optimize the CHES guide design through a parameterization that allows for a numerical optimization of neutron transport, brilliance transfer, and flux on sample with a minimization of beam divergence. Monte Carlo ray tracing programs, such as McStas^{73–75} and McStasScript,^{76,77} were used with standard numerical optimization libraries to perform these calculations.

Our new algorithm is based on the following workflow:

1. A McStas instrument file containing the STS source description for the CHES tube moderator, a set of guide any-shape component(s), and several monitors is generated for the simulation.
2. A set of real engineering constraints within STS (e.g., guide window dimensions, bunker location, gaps in the guide system, etc.) is added in the function that will generate the guide profiles. This function can model any curve, such as ellipses, parabolas, hyperbolic tangents, or hybrid curves, to study many possible profiles.
3. At the pinch points of the guide system—which for CHES corresponds to the positions of the P-chopper, M-chopper, and sample—a series of monitors are placed to detect flux, divergence, and beam profile.
4. At each cycle, the code generates a new 1D-guide profile that is then rotated n -times, where n is a parameter representing

the number of sides for a guide section, i.e., $n = 4$ for square guides, along the beam axis (\hat{z} -axis) to get the desired guide cross section. Slits located at each guide entrance avoid leaking neutrons to propagate in the system.

- Finally, the “lmfit” library⁷⁸ is used to minimize a cost function, which contains our figure of merit (FoM) for this refinement, and find the best set of parameters fed to our model function at step 2 to generate our guide system.

Notice that gravity has not been taken into consideration in this optimization and it will be included in the future.

Considering the flexibility of this approach within the framework of the guide illumination problem, we also decided to investigate what type of guide cross section provides the best neutron transport for the instrument. Thus, we varied the parameter n in the above step 4 to analyze square, hexagonal, octagonal, decagonal, and dodecagonal guide cross sections. Hexagonal and decagonal cross sections will make the horizontal(vertical) divergence asymmetric, while there is barely any difference in performances between an octagonal and dodecagonal guide, but the former is easier and less expensive to manufacture. Square guide cross sections can still be used for CHESSE, but the guide needs to be over-illuminated to avoid holes in the transported phase space.

A comparison of the main results between the square and octagonal cross section is shown in Figs. 4–6.

Our guide system has been optimized to focus the highest beam intensity on a 1 cm^2 monitor at the sample location. Figure 4 shows a comparison of the predicted phase space simulated for an octagonal

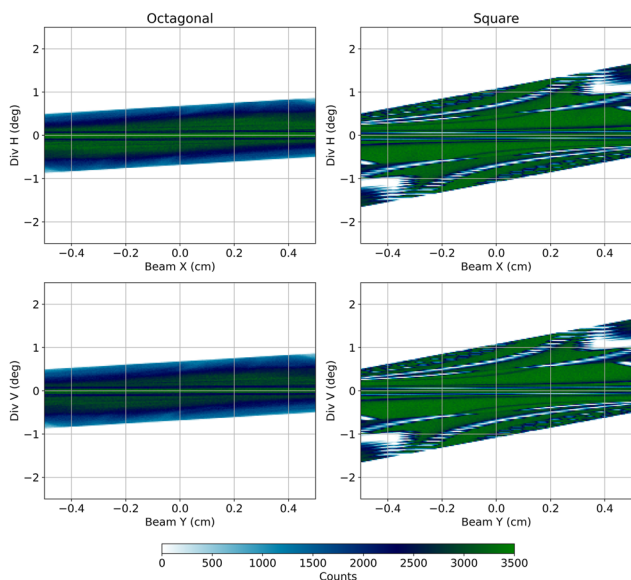


FIG. 4. Predicted phase space at the sample position. (Left) The comparison of the phase space measured at the sample position shows the absence of gaps for the octagonal guide system. The vertical(horizontal) divergence profile is completely filled and it is confined between $\pm 0.9^\circ$. (Right) The higher beam divergence of the square guide $\pm 1.5^\circ$ is severely limited in transporting short wavelengths and contains gaps in the phase space.

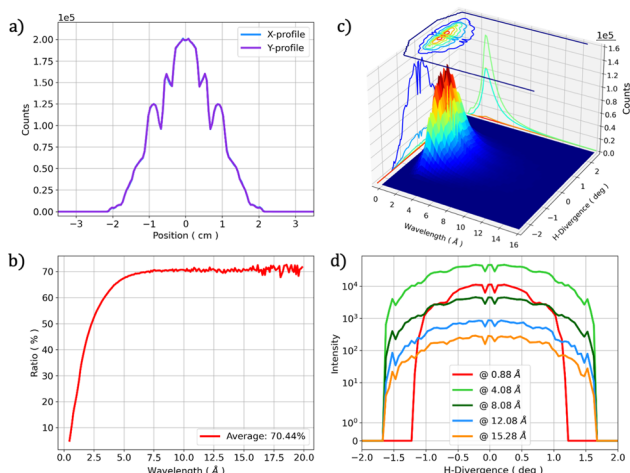


FIG. 5. Square guide performances. (a) The beam profile recorded at the sample position shows an irregular profile made of eight peaks, resulting in a non-homogeneous illumination of the sample. (b) This guide shows high neutron transport efficiency, around 70% above 6 \AA . (c) 3D monitor analyzing the divergence profile as a function of the wavelength. (d) The square guide shows a wavelength dependent divergence profile.

cross section (left) and a square cross section (right). The octagonal guide system is clearly superior and shows a continuously filled phase space, confined in $\pm 0.9^\circ$ (consistent with Ref. 70). A bigger divergence can be achieved with this guide system by tuning the profile of the closest guide to the sample, immediately after the M-chopper. This optimization will provide more flux, but it will also delocalize the beam around the center, with the risk of increasing

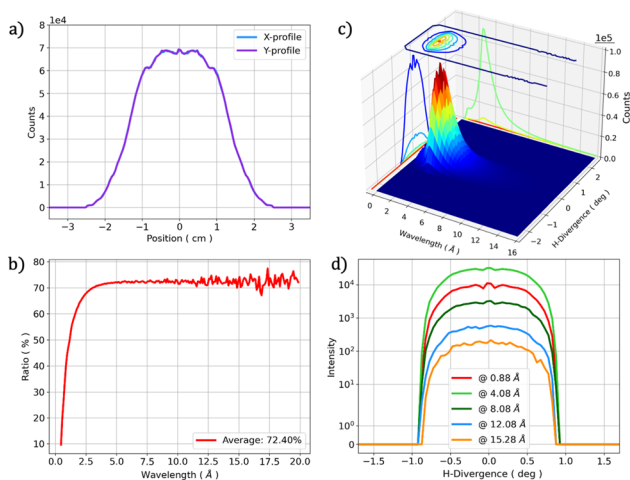


FIG. 6. Octagonal guide performances. (a) The beam profile recorded at the sample position shows a very homogeneous beam focused on $\approx 1\text{ cm}^2$ area. (b) The guide has a high neutron transport efficiency around 72.5% above 2.5 \AA . This is outstanding considering that it is obtained with a highly collimated beam divergence of $\pm 1^\circ$ and results in a wavelength independent divergence profile shown in (c) and (d).

the amount of neutrons missing the sample. The possibility of having an inter-changeable last guide section will be re-evaluated in the future within the framework of sample environments. Indeed, due to the small size of this final guide piece, we are considering the idea of customizing several of them according to the sample environment in use at the beamline.

Illuminating a square guide entrance with a circular source is akin to the proverbial “fitting a round peg into a square hole.” Either the size of the guide entrance is reduced to assure perfect illumination, which might mean losing intensity due to over-illumination, or one matches the width and height of the guide to the diameter of the moderator surface, which results in under-illumination in the corner regions of the guide. The optimization algorithm result is somewhere in between these two cases, and some holes in the phase space are clearly visible at the sample position. This has two effects visible in Fig. 5: (1) the beam profile at the sample position is very irregular and made of eight peaks. (2) The divergence profile is also non-homogeneous and wavelength dependent, and since CHES is being designed for maximum flux on small samples, any ripples in the beam profile may be problematic during the course of the measurements. This guide can transport neutrons with a predicted efficiency around 70%, as calculated by dividing the neutrons measured at the sample location by those at the entrance of the first guide.

The octagonal guide system, previously considered in Ref. 79, reaches similar neutron transport efficiency peaked around 72.5% with a beam divergence of less than $\pm 1^\circ$. This guide also results in a homogeneous beam profile [see Fig. 6(a)] and a wavelength independent divergence profile. Further comparisons of these guide systems are reported in Appendix A 1.

B. Optimization of the chopper cascade for repetition rate multiplication (RRM)

The chopper locations at STS have physical constraints due to radiation level requirements and walls that must be taken into account when building an instrument. As mentioned earlier, CHES will employ a T_0 -chopper to suppress the prompt-pulse neutrons. This chopper allows for a large wavelength band of neutrons at the instrument and will likely be a horizontal axis T_0 -chopper operating in multiples of the source frequency. As shown in Ref. 80, it is necessary to place the P- and M-choppers at commensurate positions relative to the source in order for RRM to work. Possible distance ratios to the source (P:-M-) are 1 : 2, 1 : 4, or 2 : 3. Other options, such as 1 : 3, cannot be employed at CHES without the chopper clashing with one of the wall of STS. If we follow the optimization procedure suggested in Ref. 80, we can identify the best location of the P-chopper, which will set our instrument length. Specifically, the energy resolution can be calculated from the burst times Δt_P and Δt_M at the P-chopper and the M-chopper, respectively. While these two contributions to the energy resolution are experimentally controlled by the chopper system, flight path uncertainties (Δt_D) due to the spatial extent of the neutron beam, the spatial extent of the sample, and due to uncertainties in the time and the position of neutron detection have to be taken into account. Therefore, we have

$$\delta E = \frac{h^3}{m_n^2} \frac{\sqrt{A^2 + B^2 + C^2}}{(\lambda'/\lambda)^3 L_{PM}}, \quad (4)$$

where

$$\begin{cases} A = \Delta t_M (L_{PM} + L_2 + (\lambda'/\lambda)^3 L_3), \\ B = \Delta t_P (L_2 + (\lambda'/\lambda)^3 L_3), \\ C = \frac{m_n}{h} L_{PM} \lambda' v \Delta t_D, \\ \Delta t_P = \Delta t_M \left(\frac{L_{PM}}{L_2 + (\lambda'/\lambda)^3 L_3} + 1 \right). \end{cases} \quad (5)$$

m_n is the neutron mass, h is Planck's constant, λ, λ' represent the neutron wavelength before and after scattering at the sample, respectively, and L_{PM} is the distance between P- and M-choppers.

From our analysis, the two best ratios to place the P-chopper are at 1 : 2 or 2 : 3 from the M-chopper, right outside the bunker wall of STS. The RRM mode has to be linked by the distance from the source to the respective P- and M-choppers to transmit the same wavelength periodically with the source frequency,

$$f_P = \frac{L_M}{L_P} f_M. \quad (6)$$

Considering our two possible ratios in Eq. (6) and assuming $f_M = 300$ Hz leads to $f_P = 600$ or 450 Hz. The former f_P frequency can easily be achieved by spinning the P-chopper at $f_P = 300$ Hz and doubling the number of apertures compared to the M-chopper, while achieving the latter is more complicated and our analysis showed that it could introduce some spurious energies. Thus, the 2 : 3 option was rejected. The resulting characteristics of the chopper cascade are provided in Table II.

CHES will adopt a set of two counter-rotating double-disk high-speed choppers running at 300 Hz (P-, M-choppers) and two rotating double-disk medium-speed choppers running at 15 Hz (frame overlap F-, and hand H-choppers). We anticipate borated carbon-fiber disks with standard diameter ($60 \leq \varnothing \leq 124$ cm) for the F-, P-, M-choppers, and two borated carbon-fiber disks customized ($\varnothing = 70$ cm) for the H-chopper, whose proposed design is shown in Figs. 7(a) and 7(b).

C. H-chopper configurations for the repetition rate multiplication mode

The Repetition Rate Multiplication (RRM) mode of operation enables improved efficiency for measuring large regions in energy and momentum transfer space. The H-chopper disk apertures have been revised since Ref. 67 and provide more flexibility and configurations for future experiments. Our approach is based on three key points: (1) provide the maximum number of RRM energies compatible with the $f_S = 15$ Hz of the STS source, (2) avoid overlaps between subsequent incident energies (E_i) within an energy transfer range $-2.1E_i \leq \Delta E \leq 0.9E_i$, and (3) spread the energies homogeneously across the bandwidth to provide flexibility in measurements.

Taking as a reference [Figs. 1, 7(c), and 7(d)], we color coded our chopper system for an easy visualization of the RRM mode. The F-chopper is the crimson line, the opening of the P- and M-choppers is shown with black and green markers, respectively, while the H-chopper is visualized with a cyan line. Only the incident energies that will arrive at the sample (magenta line) are shown in black.

Assuming as a starting point that the H- and M-choppers will never rotate below $f_H = 15$ Hz and $f_M = 300$ Hz, respectively,

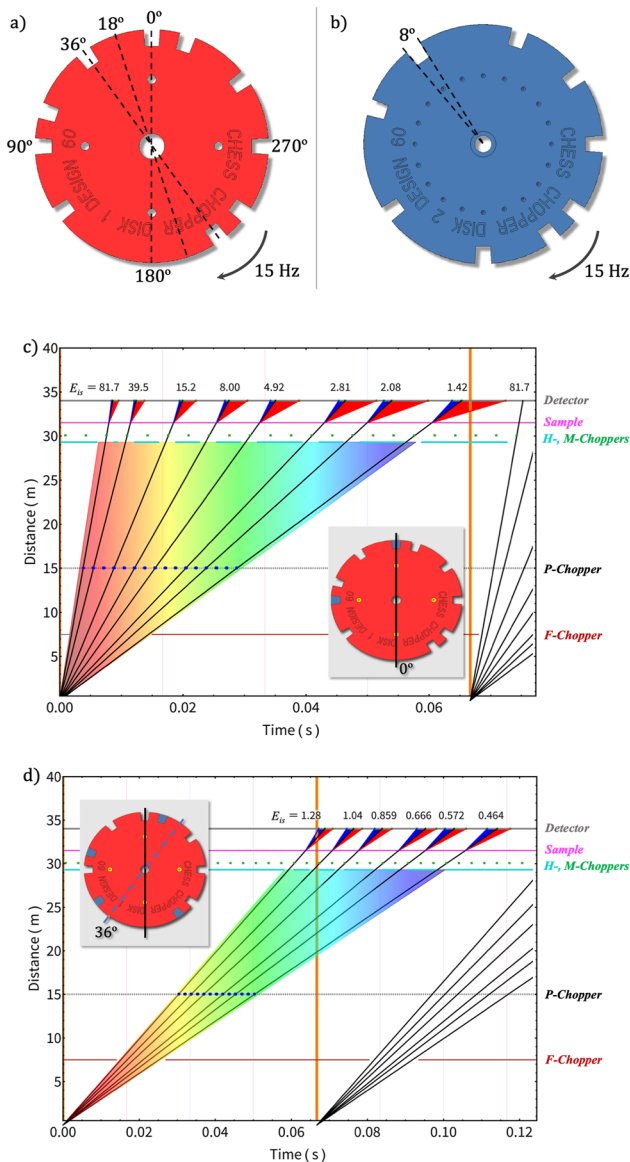


FIG. 7. H-disk chopper configurations. (a) and (b) Preliminary design of the H-chopper disks. The center of each 8° aperture is located at a multiple integer of 18° along the disks. The combinatorial analysis allows only $1 \leq E_i \leq 8$ to reach the sample with a flexible scheme when the disks are overlapped. The space-time diagrams are showing two out of 90 possible configurations of the H-chopper: (c) $8 E_i$ are hitting the sample granting no overlap in energy transfer up to $-2.1E_i \leq \Delta E \leq 0.9E_i$ (blue and red sectors). (d) $6 E_i$ are hitting the sample in the energy transfer $\Delta E = \pm 0.5E_i$. The FTS and STS pulses are shown with purple and orange vertical lines.

the natural choice to select the apertures in the H-chopper disks is to divide each of them in $300/15 = 20$ slots. This problem can be mapped into a combinatorial one if we assume that each aperture(closure) is represented by 0(1). In this way, each disk can be

uniquely identified by a 20-digit binary number, and the problem is reduced to generate all possible combinations of the two disks to find the one that best matches our three RRM criteria. Specifically, once the code has gone through all the 2^{20} possible combinations, it rules out all the ones that have more than eight apertures and those that contain zero apertures. Then, it classifies the remaining ones based on our three criteria and as a function of nominal incident wavelength. Results are reported into a matrix for easy visualization and statistically analyzed to find the best configuration. In practice, once the correct apertures of the two disks are identified, we will simply phase one with respect to the other to obtain a different set of configurations based on the experiment performed.

Our preliminary optimized disks are shown in Figs. 7(a) and 7(b); both disks will rotate clockwise at $f_H = 15$ Hz, and the center of each aperture is located at a multiple integer of 18° along the disks. Theoretically, the H-chopper should be placed as close as possible to the M-chopper to efficiently suppress unwanted E_i . In practice, there are engineering constraints due to the size of the motors of these two choppers. Thus, we analyzed two possible locations for this chopper: the current one at 29.3 m with 8° wide apertures, and a second one at 29 m with 9° wide apertures due to the wider guide profile at that location. The H-chopper will perform equally well at these positions, and it will not affect the flux or the resolution.

Figures 7(c) and 7(d) show space-time diagrams that represent two out of 90 possible configurations for the RRM mode. One shows the H-chopper phased to obtain eight incident energies, E_i , hitting the sample without any overlaps in our selected energy transfer range. The second shows the H-chopper phased for a longer wavelength to obtain $6E_i$ hitting the sample without overlap in the energy transfer $\Delta E = \pm 0.5E_i$. This could be a very useful configuration for QENS measurements. With the chosen chopper configuration and the $f_S = 15$ Hz of the STS source, CHES will be able to employ a maximum of eight RRM energies with no overlap between them.

In order to test this device, we have already 3D-printed mock-up disks of Figs. 7(a) and 7(b) at the 1:5 scale. Such flexible configurations are achieved in reality in two steps: (1) we first phase the second disk with respect to the first one to select the maximum number of openings. (2) Once locked, the two disks will rotate like a single body and we will phase them based on the nominal incident energy we want to measure and how we want to spread the energy across our bandwidth. Software will take care of cropping and reducing the final dataset based on our chopper settings. Possible other H-chopper layouts will be also considered as CHES progresses.

D. Optimization of the fast P- and M-choppers

Using McStas and MCViNE software, we were able to optimize our fast P- and M-chopper apertures to suppress some of the artifacts affecting the elastic line. Specifically, we optimized the width of each aperture in these choppers to avoid the Ikeda tail⁴⁷ in the neutron energy gain side of the spectrum. This will provide a more symmetric energy resolution function and help facilitate the analysis of QENS measurements. Using a similar workflow as the one described in Sec. IV A, we fit the calculated elastic line as a function of incident energies and angular opening for these two choppers. Our results showed that the P-chopper and M-chopper must have a maximum opening angle of 40° and 8° , respectively. We observed that the

P-chopper is most responsible for causing the Ikeda tail, and its openings greatly affect the flux, whereas the M-chopper configuration has less impact on the shape and the extent of the tail but greatly affects both flux and resolution. For this reason, we concluded that it is in the best interest of the science case to have the possibility to re-phase the M-chopper to increase the energy resolution. We refer to this mode of operation as High Resolution (HR), and it can be efficiently realized by decreasing the M-chopper opening angle to 6° .

The blind chopper solution proposed by the Versatile Optimal Resolution (VOR) instrument^{81,82} was also taken into account in this analysis, despite the shorter pulse of STS when compared to ESS.⁸³ Our simulations did not give us meaningful results to justify the cost and space requirements in the guide system for this technique, so it was discarded.

E. 3D-printed radial collimator, slits, and shields

Incident and scattered beam collimation have been preliminary considered for the CHES instrument. Details of collimation choices will be presented in future publications. Considering the different size of each sample environment proposed in Sec. III B, we are proposing that scattered beam radial collimators are made for each sample environment used at the instrument. This allows for customization of the blade spacing and collimator inner and outer radii for each particular sample environment. This is the same solution currently used at AMATERAS,^{84,85} where the radial collimator is mounted directly on sample environments. In our design, we also included the possibility to swap the collimators between different instruments to match different detector geometries. This optimization will be based on the works done in Refs. 86–91.

The octagonal guide cross section and the resulting circular beam cross section are not well matched to current off-the-shelf slit packages. For CHES, the beam size needs to be changed $1 \leq \varnothing \leq 22$ mm. Solutions being studied range from circular apertures translated into the beam to an *iris* mechanism⁹² inspired by circular camera shutters.

V. ANALYSIS OF THE DETECTOR SYSTEM

The CHES detector array will reach a solid angle coverage of $\Omega = 2\pi$ sr. This is achieved by placing the detectors on a spherical frame as shown in Fig. 8(a). Compared to the more traditional cylindrical arrangement, the spherical configuration is more compact, and it can reach higher out of plane coverage with a smaller number of detectors. As the instrument is currently in the preliminary design phase, we are also evaluating a cylindrical configuration. Specifically, we are comparing resolution ellipsoids⁹³ as a function of sample shape, incident energy, and different chopper configurations and comparing the two geometries when symmetry operations are applied to the resulting data. Regardless of the final detector configuration, the CHES detectors consist of ^3He Linear-Position-Sensitive-Detectors (LPSD) arranged in the standard ORNL eight-pack configurations. Details are provided in Table III. These detectors are commercially produced as tubes with a circular cross section or with a more custom design.⁹⁴

Each eight-pack consists of an ensemble of 8, 1.5 m long, 2.54 cm (1 in.) diameter tubes, filled with 8 bar of ^3He that will grant

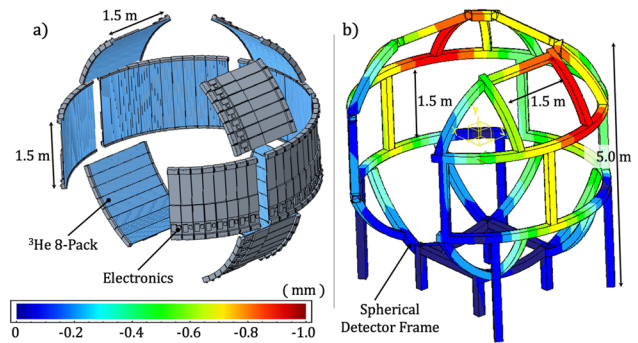


FIG. 8. CHES detector layout and frame. (a) Spherical arrangement of the 95 eight-pack detectors. (b) FEA analysis of the detector frame showing the points with maximum deflection along the vertical y -axis. Based on the material, the maximum deflection is estimated to be $0.4 \leq y \leq 0.9$ mm.

an efficiency $>90\%$ for the energy range in use at CHES. A tube longer than 1.5 m may result in a deformation that will change the pixel distance from the sample and would not fit in the tank. Cross-talk between detectors on the opposite sides of the frame and among neighboring tubes is a potential concern, and it will be evaluated with future simulations. The spherical geometry can host 95 detectors divided in seven major arcs: the mid-plane arc grants an in-plane coverage $-140^\circ \leq 2\theta \leq 140^\circ$ and an out-of-plane $-16^\circ \leq \phi \leq 16^\circ$. The out-of-plane coverage is then extended with six (three top and three bottom) arcs located at $2\theta = 0^\circ$ and $\pm 90^\circ$ to $-55^\circ \leq \phi \leq 55^\circ$. The cylindrical configuration consists of a repetition of the main in-plane arc for the top and bottom ones. This configuration can host a total of 171 8-packs, with a similar solid angle coverage.

LPSD are characterized by high reliability, with a high signal-to-noise ratio and very low sensitivity to gamma rays⁹⁵ and fast neutrons.⁹⁶ A possible drawback is related to the significant charge collection time that limits the ability to adequately process multiple simultaneous events detected across the tube.⁹⁷ This should not present an issue for the spectrometer since the saturation will probably be reached only for high intensity features, such as Bragg reflections. Incident beam attenuators will be available on motorized stages in order to mitigate this issue when a quantitative measure of Bragg peak intensity is required.

TABLE III. CHES detector specifications. LPSD: linear position sensitive detector.

Parameter	Description
Tube length	1.5 m
Tube diameter	2.54 cm
Tube material	Stainless steel
Tube thickness	0.5 mm
L_3 distance	2.5 m
Detector type	^3He LPSD
Detector arrangement	8-pack, linear
^3He pressure	8 bar
Number of pixels	$128 \times 8 = 1024$
Number of 8-packs	95

Figure 8(b) shows the outcome of the Finite Element Analysis (FEA) performed on the structure to identify deformations due to gravity, which may change the detector(pixel) positions. The calculation has been performed with the software CREO Parametric assuming an Al6061 detector frame and a total weight for each individual 8-pack of 50 lb (≈ 23 Kg) that accounts for electronics and shielding material. Most of the deformation is present in the upper arcs (red area) along the vertical direction \hat{y} , and it is close to 0.89 mm. Changing the material of the detector frame from Al to non-magnetic stainless steel (SS) 304 reduces the shift down to 0.45 mm. Monte Carlo simulations analyzing the effects of these shifts and other random pixel misalignments are currently ongoing. Detector positions in the as-built instrument will be refined based upon measurements of standard samples at the start of each measurement cycle.

A. Monitors

A set of beam monitors⁹⁸ will be installed across the 34 m of the beamline to study and track the behavior of the instrument during operations. The collected data will be used for diagnostic purposes. The beam monitors will also be used to refine the incident energies of the instrument assisting in the parallel reduction of the RRM data.

CHES will be equipped with at least five time of flight (ToF) monitors: three movable monitors located right after the F-, P-, and H-chopper for diagnostic measurements, and two fixed right after the M-chopper and in the beam-stop to measure accurately the incident energies. Details related to the monitor type are currently being evaluated, and R & Ds are already in place to evaluate different technologies.

For instrument commissioning and calibrations, there will be another monitor installed at the sample position to measure neutron flux. This measurement will also serve to compare our Monte Carlo simulations for both tube moderator performances and guide efficiency with reality. An area monitor in this position will be especially useful to measure beam homogeneity under different chopper and aperture conditions.

CHES is designed to target measurements of very small samples, ≈ 1 mm³; thus, mechanisms must be in place to both tailor and monitor the beam size and the sample position. A transmission camera will be telescoped into position to allow one to accurately set the beam aperture. The sample position will need to be able to be adjusted vertically as well as in the horizontal plane. Vertical translation is regularly achieved in current sample environments, while horizontal translation will likely be performed with piezo-motors. Smaller samples can instead be aligned using a laser beam similar to what the Spallation Neutrons and Pressure Diffractometer (SNAP) beamline is currently achieving. The choice of these devices is entangled with the sample environment geometry, so it will be investigated carefully at a later stage of the project.

VI. VIRTUAL EXPERIMENTS

The CHES performance has been investigated with a series of Monte Carlo simulations employing MCViNE. Several science cases have been simulated using both a monochromatic beam and in RRM mode, and the data have been analyzed with standard Mandrid algorithms. For this preliminary design phase, we did not include

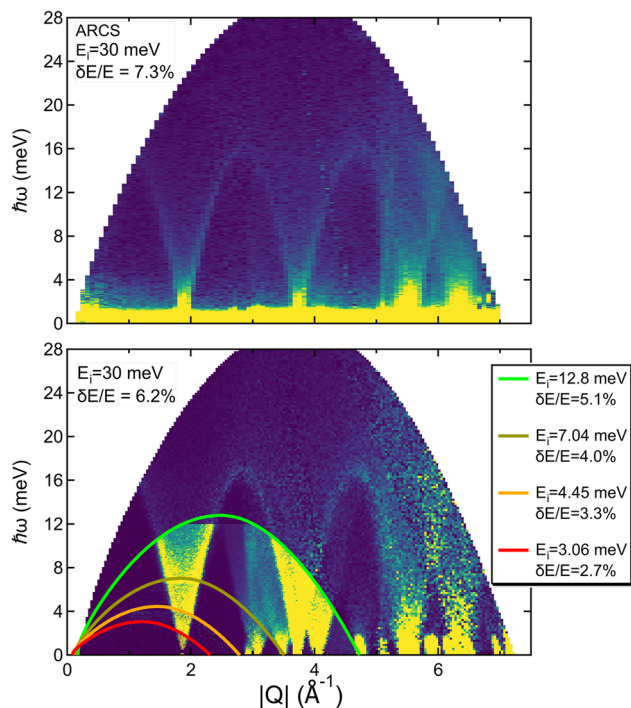


FIG. 9. RRM mode applied to poly-crystalline graphite. Comparison of a simulated poly-crystalline graphite sample (bottom) using RRM mode with five energies and the real dataset measured at ARCS. CHES can measure simultaneously five dataset with increasing energy resolution that can be combined together and analyzed with super-resolution techniques.

multiple scattering or other background effects in our scattering kernels.

Figure 9 shows the comparison of a simulated poly-crystalline graphite in the RRM mode (bottom), compared with real data collected at ARCS (top) at $E_i = 30$ meV.⁹⁹ Our simulation captures the phonon dispersion of the graphite with similar energy resolution to the ARCS instrument. However, in a single measurement, CHES is able to capture four more incident energies with increasingly better resolution as the wavelength increases. These data can then be analyzed individually or merged in order to use super-resolution analysis techniques.¹⁰⁰

A similar result is shown in Fig. 10 where we simulated a $m = 1$ mg single crystal sample of $K_2V_3O_8$, phasing the H-chopper for two energies $E_i = 5.11$ and 1.05 meV. Details on the physics of this system can be viewed in Ref. 101. This simulation highlights the versatility and capabilities of CHES; by virtue of the RRM mode, CHES is able to simultaneously measure the entire bandwidth of the excitation and to resolve a 81 μ eV gap in the spectrum (inset). The calculated spectrum also illustrates that CHES does have a finite energy and wave-vector resolution that varies and *tilts* across the large detector array. This can be seen in the filled portion of the measured scattering intensity near the (100) and (300) wave-vectors. This four-dimensional resolution ellipsoid is intrinsic to all

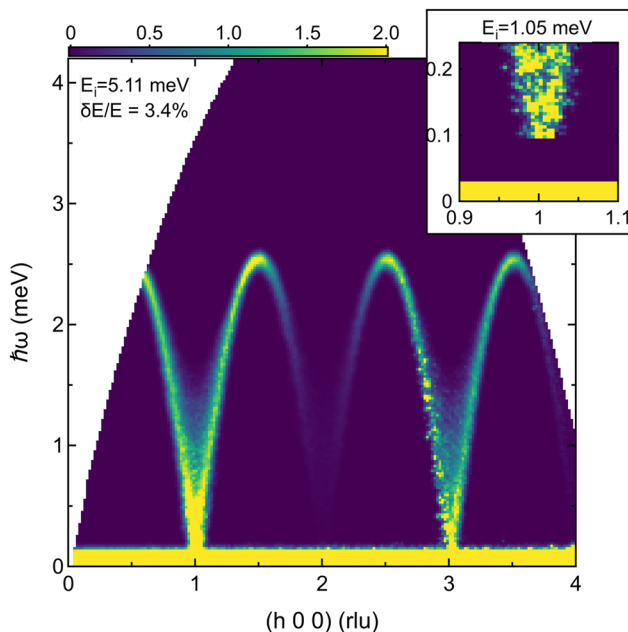


FIG. 10. Simulated single crystal data of $K_2V_3O_8$. The simulation of $m = 1$ mg sample of $K_2V_3O_8$ clearly demonstrates that CHES resolution is able to measure the 81 μeV gap along (100) at the same time as the main dataset. Results also highlight the effect of a non-focusing resolution ellipsoid on the spin wave branch along (300).

neutron spectrometers, and the ability to characterize it with numerical calculations will allow future measurements to more accurately be compared to theoretical models.

VII. SUMMARY

Combining several innovative computational techniques, we were able to optimize the performance of the CHES instrument. Its ability to measure up to eight energies simultaneously in the RRM mode without significant overlaps in one frame, coupled with the possibility to trade flux for resolution by appropriate phasing the fast double disk choppers, will aid in the rapid characterization of emergent materials. The high flux will also be fundamental for polarization analysis, which is currently a difficult and very time consuming technique to employ. Indeed, polarization capabilities are currently being evaluated, and they will be the subject of a future publication.

CHES is poised to be the next flagship cold neutron spectrometer in the world, and it will leverage on the experience of all his older siblings to manipulate flux for highly customized measurements.

ACKNOWLEDGMENTS

G.S. acknowledges useful discussions with A. Khaplanov (ORNL), P. Deen (ESS), R. Bewley (ISIS), K. Kaneko, S. Ohira-Kawamura and K. Nakajima (J-PARC), and M. Janoschek (PSI). G.S. is also very grateful to all users who supported CHES during the STS instrument selection process. Work at ORNL's Spallation Neutron Source by G.S., C.B., A.D.C., C.L.H., D.N.K.,

J.Y.Y.L., M.D.L., D.G.Q., and M.B.S. was supported by the Scientific User Facilities Division, Office of Basic Energy Sciences, U.S. Department of Energy (DOE). Work by A.D.C., R.P.H., and M.E.M. was supported by the U.S. Department of Energy, Office of Science, Basic Energy Sciences, Materials Sciences and Engineering Division.

This manuscript has been authored by UT-Battelle, LLC under Contract No. DE-AC05-00OR22725 with the U.S. Department of Energy. The United States Government retains and the publisher, by accepting the article for publication, acknowledges that the United States Government retains a non-exclusive, paid-up, irrevocable, world-wide license to publish or reproduce the published form of this manuscript, or allow others to do so, for United States Government purposes. The Department of Energy will provide public access to these results of federally sponsored research in accordance with the DOE Public Access Plan (<http://energy.gov/downloads/doe-public-access-plan>).

AUTHOR DECLARATIONS

Conflict of Interest

The authors have no conflicts to disclose.

Author Contributions

G. Sala: Conceptualization (equal); Data curation (equal); Formal analysis (equal); Supervision (equal); Writing – original draft (equal); Writing – review & editing (equal). **M. Mourigal:** Writing – original draft (equal); Writing – review & editing (equal). **C. Boone:** Writing – review & editing (equal). **N. P. Butch:** Writing – review & editing (equal). **A. D. Christianson:** Writing – review & editing (equal). **O. Delaire:** Writing – review & editing (equal). **A. J. DeSantis:** Writing – review & editing (equal). **C. L. Hart:** Writing – review & editing (equal). **R. P. Hermann:** Writing – review & editing (equal). **T. Huegle:** Formal analysis (equal); Writing – original draft (equal); Writing – review & editing (equal). **D. N. Kent:** Writing – review & editing (equal). **J. Y. Y. Lin:** Writing – review & editing (equal). **M. D. Lumsden:** Writing – review & editing (equal). **M. E. Manley:** Writing – review & editing (equal). **D. G. Quirinale:** Writing – review & editing (equal). **M. B. Stone:** Writing – review & editing (equal). **Y. Z:** Writing – review & editing (equal).

DATA AVAILABILITY

The data that support the findings of this study are available from the corresponding author upon reasonable request.

APPENDIX A: MATHEMATICAL FORMALISM USED FOR GUIDE OPTIMIZATIONS

We report here the three main functions used to generate the guide profiles of the CHES instrument. The 31 m of guide system can be divided into three distinct sections that can be optimized separately or simultaneously: (1) a 14.2 m guide from the moderator window to the P-chopper, (2) a 14.9 m guide from the P-chopper to the M-chopper, and (3) a 1 m guide from the M-chopper until 50 cm before the sample as shown in Fig. 11. Those 50 cm are left to account for the biggest radius of our sample environments, but future optimizations may bring the guide even closer or inside these devices. The three ellipsoids that represent the guide system are

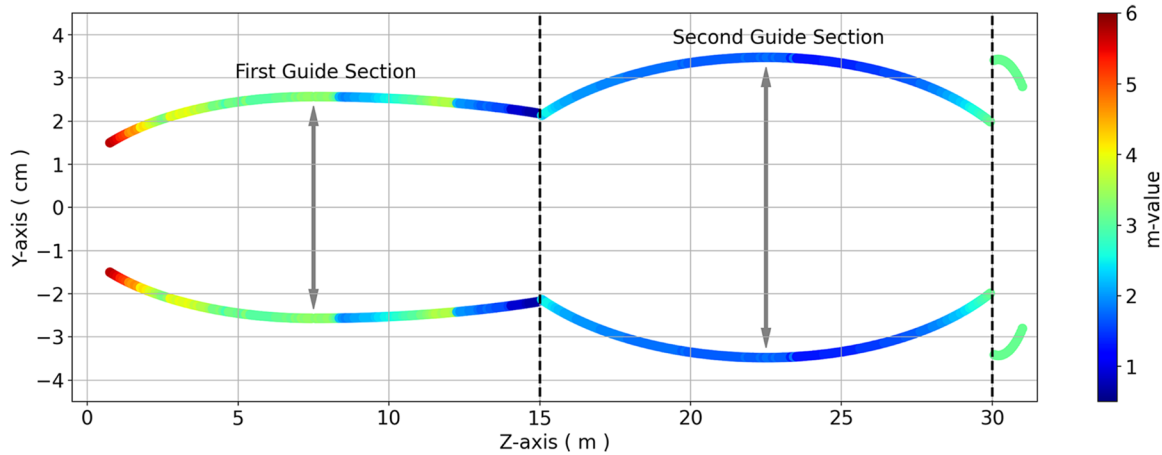


FIG. 11. CHESSE guide layout. A projection on the YZ-plane showing the profiles of the three guide sections. Color matches the m -value of the super-mirror at that location. Vertical dashed lines are guides to the eye showing the location of the P- and M-chopper where the guides are pinched. The third section ($|z| \geq 30$ m) can be switched based on the sample environment in use as explained in the main text.

$$f(z) = \begin{cases} b_1 \sqrt{1 - \left(\frac{7.5 - z}{a_1}\right)^2} & \text{for } 0.75 \leq |z| \leq 15 \text{ m,} \\ b_2 \sqrt{1 - \left(\frac{22.5 - z}{a_2}\right)^2} & \text{for } 15 \leq |z| \leq 30 \text{ m,} \\ b_3 \sqrt{1 - \left(\frac{30.2 - z}{a_3}\right)^2} & \text{for } |z| \geq 30 \text{ m,} \end{cases} \quad (\text{A1})$$

where a_i and b_i correspond to the semi-major(minor) axes of the ellipses, respectively, and \hat{z} -axis is along the beam. Each one of these curve can be separated at the mid-point to account for hybrid profiles. Furthermore, since the guide_ anyshape component in McStas handles “off” files, which are arrays of points, our program can also include gaps for Al windows, chopper housing, shutters, etc., when generating the profiles.

Indeed, as shown in Ref. 70, having a single perfect ellipse does not provide the best neutron transport, so we investigated many different hybrid functions during the early design of the guide system. The final guide profile is shown in Fig. 11, where we highlight the ellipsoidal shape of the guide, wider at the center than at the extremes, and the pinch point at the P- and M-chopper locations (dashed black line). The projection in the YZ-plane is also color coded based on the optimized m -value of each super-mirror as explained in Appendix A 1. Our simulations showed that the profile of the third guide section, $|z| \geq 30$ m, affects dramatically the beam divergence profile hence the flux. For this reason, we are considering the possibility to swap and optimize this guide based on the sample environment used.

Overall, the first section focal points are located behind the tube moderator and almost at the midpoint of the second guide, while the second section is more similar to a perfect ellipse. These shapes can take care of aberrations like coma very efficiently, resulting in a filled phase space and a wavelength independent divergence (see the main text).

1. Preliminary analysis on the guide coating

An important parameter that defines the guide efficiency and its cost is the number of reflective coating layers, expressed as

m -values,⁶⁸ assigned to each super-mirror in the guide. Our preliminary analysis is done using a tally component in McStas¹⁰² that can keep track of the number of neutron bounces along the guide system as well as the reflection characteristics of each bounce. Theoretically, the lower the number of bounces, the higher the flux and hence the efficiency in the neutron transport.

Once fully optimized, both the square and octagonal cross section guides have been analyzed using this tally component. Figure 12 reports histograms showing the distribution of the number of neutron bounces for an octagonal (left) and a square (right) guide system. Once again the octagonal cross section is far superior to the square one. In the former case, on average, neutrons just bounce 3–4 times maximum before reaching the sample, while the latter case requires at least 7–8 bounces. Based on these data, we estimated that the octagonal guide system should have on average an $m = 2$, while the square guide an average $m = 3$ as shown in Fig. 12. These results are still preliminary and require further simulations.

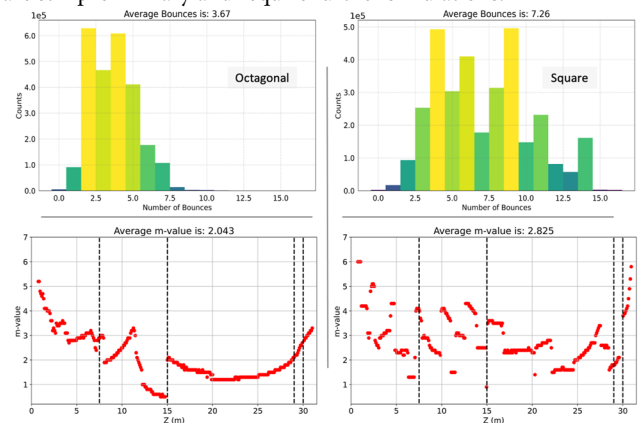


FIG. 12. Analysis of neutron trajectories. Top: Histograms comparing the number of neutron bounces for octagonal and square guide cross sections. The average bounces from the moderator to sample are 4 and 7, respectively. Bottom: Estimated m -values for each guide element across the full instrument. Vertical dashed lines represent the locations of the choppers.

APPENDIX B: CALCULATION OF THE CHOPPER OPENING TIMES

We report here the mathematical formalism used to develop the H-chopper analysis described in Sec. IV C.

As stated in the main text, we uniquely identify the 20 possible apertures or closures on the H-chopper disk with a 0 or 1, respectively. Mapping this combinatorial problem on a simple 20-digit integer array helps to speed up the calculation and allow us to use basic functions to generate all the possible combinations that represent the disk overlap. For example, we can rotate the disk by an angle $\theta = n \times 18^\circ$ (counterclockwise) by cycling the elements of our array n position to the left(right). Furthermore, given two 20-digit integer arrays representing our disks, $Y_{1,2}$, their overlap and final number of apertures can be calculated as

$$Y_1 + Y_2 = \text{Ceiling}\left(\frac{Y_1 + Y_2}{2}\right), \quad (\text{B1})$$

where the ceiling function returns the smallest integer greater than or equal to x . This function makes sure that only when two zeros (apertures) in the arrays are summed the result is always a zero or one in all the other cases.

The energy and the wavelength of the neutron are related as

$$E_i = \frac{81.7452}{\lambda_i^2}, \quad (\text{B2})$$

with E_i in meV and λ_i in Å. Once a final subset of combinations is identified based on our criteria, we can then calculate the opening time of the chopper for the nominal wavelength as

$$t_{\text{open}} = d/v, \quad (\text{B3})$$

where d is the chopper distance from the moderator and $v = \sqrt{2E_i/m_n}$ the velocity of the neutron. The chopper velocity is given by

$$\omega = 2\pi R f n_{\text{disk}}, \quad (\text{B4})$$

where R is the chopper radius, f its frequency, and n_{disk} the number of disks.

The total full opening time depends on the chopper typology according to

$$t_{\text{full}} = \frac{w(\alpha)_{\text{aperture}} + w(z)_{\text{guide}}}{\omega}, \quad (\text{B5})$$

where $w(\alpha)_{\text{aperture}} = 2\pi R(\alpha/360)$ and $w(z)_{\text{guide}}$ are the width of the chopper aperture (α in degree), and the guide width at that location (z), respectively. Note that, for counter-rotating double disk choppers, Eq. (B5) needs to be divided by two.

Finally, the minimum(maximum) opening time of the chopper used to generate our space-time diagrams is

$$t_{\text{min}}, t_{\text{max}} = t_{\text{open}} \mp \frac{t_{\text{full}}}{2}. \quad (\text{B6})$$

The cross-talking between the two pairs of rotating disks can be studied following the formalism in Refs. 103–105.

APPENDIX C: LAYOUT OF THE CHESSE SPECTROMETER AND ITS BACK-END

Figures 13 and 14 show the full engineering layout of the CHESSE spectrometer.

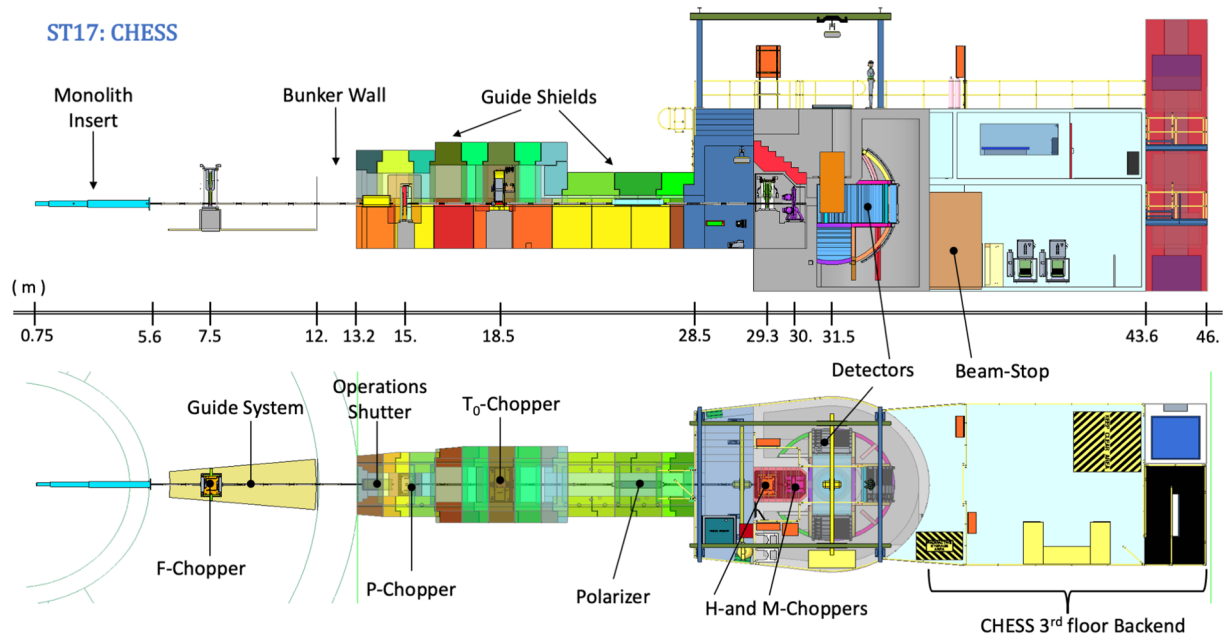


FIG. 13. CHESSE engineering layout. CHESSE has a total flight-path of 34 m from moderator to detectors. The double disks choppers, P-chopper and M-chopper, are located at the pinch points of the guide system at 15 and 30 m, respectively, while the frame-overlap (F-chopper), T-zero (T_0), and hand (H-chopper, controlling RRM) choppers are placed at 7.5, 18.5, and 29.3 m, respectively. Sample is located at 31.5 m. CHESSE is located in the 50 m wing of STS, overlooking the tube moderator beam-port ST17.

ST17: CHESSE

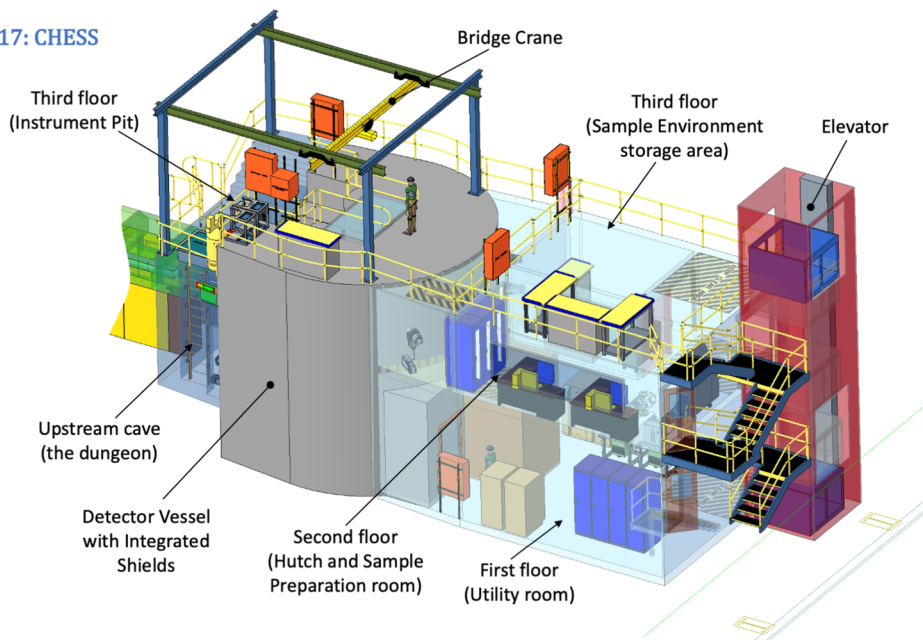


FIG. 14. CHESSE back-end engineering layout. The back-end of the instrument is designed as a three floor building, housing: a utility room for the detector vacuum system and control racks on the first floor, the instrument control center and a sample preparation laboratory for non-irradiated materials on the second floor, the sample environment storage area, and the access to the instrument on the third floor. An elevator to transport materials and equipment will serve all the three floors, while a bridge (not shown) and a staircase will allow users and ORNL staff to move across the floors and onto the STS mezzanine.

REFERENCES

- ¹M. Nakamura, K. Nakajima, R. Kajimoto, and M. Arai, "Utilization of multiple incident energies on cold-neutron disk-chopper spectrometer at J-PARC," *J. Neutron Res.* **15**(1), 31–37 (2007).
- ²M. Nakamura, R. Kajimoto, Y. Inamura, F. Mizuno, M. Fujita, T. Yokoo, and M. Arai, "First demonstration of novel method for inelastic neutron scattering measurement utilizing multiple incident energies," *J. Phys. Soc. Jpn.* **78**(9), 093002 (2009).
- ³M. Russina and F. Mezei, "First implementation of repetition rate multiplication in neutron spectroscopy," *Nucl. Instrum. Methods Phys. Res., Sect. A* **604**(3), 624–631 (2009).
- ⁴M. Russina and F. Mezei, "Implementation of repetition rate multiplication in cold, thermal and hot neutron spectroscopy," *J. Phys.: Conf. Ser.* **251**, 012079 (2010).
- ⁵A. M. Gaspar, S. Busch, M.-S. Appavou, W. Haeussler, R. Georgii, Y. Su, and W. Doster, "Using polarization analysis to separate the coherent and incoherent scattering from protein samples," *Biochim. Biophys. Acta, Proteins Proteomics* **1804**, 76–82 (2010).
- ⁶G. Sala, M. B. Stone, B. K. Rai, A. F. May, P. Laurell, V. O. Garlea, N. P. Butch, M. D. Lumsden, G. Ehlers, G. Pokharel, A. Podlesnyak, D. Mandrus, D. S. Parker, S. Okamoto, G. B. Halász, and A. D. Christianson, "Van Hove singularity in the magnon spectrum of the antiferromagnetic quantum honeycomb lattice," *Nat. Commun.* **12**, 171 (2021).
- ⁷G. Sala, M. B. Stone, B. K. Rai, A. F. May, D. S. Parker, G. B. Halász, Y. Q. Cheng, G. Ehlers, V. O. Garlea, Q. Zhang, M. D. Lumsden, and A. D. Christianson, "Crystal field splitting, local anisotropy, and low-energy excitations in the quantum magnet YbCl₃," *Phys. Rev. B* **100**, 180406 (2019).
- ⁸C. Balz, B. Lake, J. Reuther, H. Luetkens, R. Schönemann, T. Herrmannsdörfer, Y. Singh, A. T. M. Nazmul Islam, E. M. Wheeler, J. A. Rodriguez-Rivera, T. Guidi, G. G. Simeoni, C. Baines, and H. Ryll, "Physical realization of a quantum spin liquid based on a complex frustration mechanism," *Nat. Phys.* **12**, 942–949 (2016).
- ⁹A. Kitaev, "Anyons in an exactly solved model and beyond," *Ann. Phys.* **321**(1), 2–111 (2006), part of the Special Issue: January Special Issue.
- ¹⁰L. Balents, "Spin liquids in frustrated magnets," *Nature* **464**, 199–208 (2010).
- ¹¹S. Mühlbauer, B. Binz, F. Jonietz, C. Pfleiderer, A. Rosch, A. Neubauer, R. Georgii, and P. Böni, "Skyrmion lattice in a chiral magnet," *Science* **323**(5916), 915–919 (2009).
- ¹²I. Martin and C. D. Batista, "Itinerant electron-driven chiral magnetic ordering and spontaneous quantum Hall effect in triangular lattice models," *Phys. Rev. Lett.* **101**, 156402 (2008).
- ¹³Y. Kamiya and C. D. Batista, "Magnetic vortex crystals in frustrated mott insulator," *Phys. Rev. X* **4**, 011023 (2014).
- ¹⁴A. O. Leonov and M. Mostovoy, "Multiply periodic states and isolated skyrmions in an anisotropic frustrated magnet," *Nat. Commun.* **6**, 8275 (2015).
- ¹⁵J. Orenstein and A. J. Millis, "Advances in the physics of high-temperature superconductivity," *Science* **288**(5465), 468–474 (2000).
- ¹⁶P. A. Lee, N. Nagaosa, and X.-G. Wen, "Doping a Mott insulator: Physics of high-temperature superconductivity," *Rev. Mod. Phys.* **78**, 17–85 (2006).
- ¹⁷C. Pfleiderer, "Superconducting phases of *f*-electron compounds," *Rev. Mod. Phys.* **81**, 1551–1624 (2009).
- ¹⁸O. Delaire, J. Ma, K. Marty, A. F. May, M. A. McGuire, M.-H. Du, D. J. Singh, A. Podlesnyak, G. Ehlers, M. D. Lumsden, and B. C. Sales, "Giant anharmonic phonon scattering in PbTe," *Nat. Mater.* **10**, 614–619 (2011).
- ¹⁹C. W. Li, J. Hong, A. F. May, D. Bansal, S. Chi, T. Hong, G. Ehlers, and O. Delaire, "Orbitally driven giant phonon anharmonicity in SnSe," *Nat. Phys.* **11**, 1063–1069 (2015).
- ²⁰M. E. Manley, O. Hellman, N. Shulumba, A. F. May, P. J. Stonaha, J. W. Lynn, V. O. Garlea, A. Alatas, R. P. Hermann, J. D. Budai, H. Wang, B. C. Sales, and A. J. Minnich, "Intrinsic anharmonic localization in thermoelectric PbSe," *Nat. Commun.* **10**, 1928 (2019).
- ²¹Y. Zheng, T. Lu, M. M. H. Polash, M. Rasoulianboroujeni, N. Liu, M. E. Manley, Y. Deng, P. J. Sun, X. L. Chen, R. P. Hermann, D. Vashaev, J. P. Heremans, and H. Zhao, "Paramagnon drag in high thermoelectric figure of merit Li-doped MnTe," *Sci. Adv.* **5**(9), eaat9461 (2019).
- ²²W. Paulus, H. Schober, S. Eibl, M. Johnson, T. Berthier, O. Hernandez, M. Ceretti, M. Plazenet, K. Conder, and C. Lamberti, "Lattice dynamics to trigger low temperature oxygen mobility in solid oxide ion conductors," *J. Am. Chem. Soc.* **130**, 16080–16085 (2008).
- ²³M. Li, Z. Rhodes, J. R. Cabrera-Pardo, and S. D. Minter, "Recent advancements in rational design of non-aqueous organic redox flow batteries," *Sustainable Energy Fuels* **4**, 4370–4389 (2020).

- ²⁴W. Wang, Q. Luo, B. Li, X. Wei, L. Li, and Z. Yang, "Recent progress in redox flow battery research and development," *Adv. Funct. Mater.* **23**(8), 970–986 (2013).
- ²⁵Z. Rhodes, J. R. Cabrera-Pardo, M. Li, and S. D. Minter, "Electrochemical advances in non-aqueous redox flow batteries," *Isr. J. Chem.* **61**(1–2), 101–112 (2021).
- ²⁶L. A. Robertson, Z. Li, Y. Cao, I. A. Shkrob, M. Tyagi, K. C. Smith, L. Zhang, J. S. Moore, and Y. Z., "Observation of microheterogeneity in highly concentrated nonaqueous electrolyte solutions," *J. Am. Chem. Soc.* **141**, 8041–8046 (2019).
- ²⁷J. D. Nickels, H. O'Neill, L. Hong, M. Tyagi, G. Ehlers, K. L. Weiss, Q. Zhang, Z. Yi, E. Mamontov, J. C. Smith, and A. P. Sokolov, "Dynamics of protein and its hydration water: Neutron scattering studies on fully deuterated GFP," *Biophys. J.* **103**, 1566–1575 (2012).
- ²⁸J. D. Nickels, S. Chatteerjee, C. B. Stanley, S. Qian, X. Cheng, D. A. A. Myles, R. F. Standaert, J. G. Elkins, and J. Katsaras, "The in vivo structure of biological membranes and evidence for lipid domains," *PLoS Biol.* **15**, e2002214 (2017).
- ²⁹S. Perticaroli, G. Ehlers, C. B. Stanley, E. Mamontov, H. O'Neill, Q. Zhang, X. Cheng, D. A. A. Myles, J. Katsaras, and J. D. Nickels, "Description of hydration water in protein (green fluorescent protein) solution," *J. Am. Chem. Soc.* **139**, 1098–1105 (2017).
- ³⁰D. B. Anunciado, V. P. Nyugen, G. B. Hurst, M. J. Doktycz, V. Urban, P. Langan, E. Mamontov, and H. O'Neill, "In vivo protein dynamics on the nanometer length scale and nanosecond time scale," *J. Phys. Chem. Lett.* **8**, 1899–1904 (2017).
- ³¹J. D. Nickels, S. Perticaroli, H. O'Neill, Q. Zhang, G. Ehlers, and A. P. Sokolov, "Coherent neutron scattering and collective dynamics in the protein, GFP," *Biophys. J.* **105**, 2182–2187 (2013).
- ³²T. Burankova, R. Hempelmann, A. Wildes, and J. P. Embs, "Collective ion diffusion and localized single particle dynamics in pyridinium-based ionic liquids," *J. Phys. Chem. B* **118**, 14452–14460 (2014).
- ³³D. A. Turton, H. M. Senn, T. Harwood, A. J. Lapthorn, E. M. Ellis, and K. Wynne, "Terahertz underdamped vibrational motion governs protein-ligand binding in solution," *Nat. Commun.* **5**, 3999 (2014).
- ³⁴R. Ashkar, H. Z. Bilheux, H. Bordallo, R. Briber, D. J. E. Callaway, X. Cheng, X.-Q. Chu, J. E. Curtis, M. Dadmun, P. Fenimore, D. Fushman, F. Gabel, K. Gupta, F. Herberle, F. Heinrich, L. Hong, J. Katsaras, Z. Kelman, E. Kharlampieva, G. R. Kneller, A. Kovalevsky, S. Krueger, P. Langan, R. Lieberman, Y. Liu, M. Losche, E. Lyman, Y. Mao, J. Marino, C. Mattos, F. Meilleur, P. Moody, J. D. Nickels, W. B. O'Dell, H. O'Neill, U. Perez-Salas, J. Peters, L. Petridis, A. P. Sokolov, C. Stanley, N. Wagner, M. Weinrich, K. Weiss, T. Wymore, Y. Zhang, and J. C. Smith, "Neutron scattering in the biological sciences: Progress and prospects," *Acta Crystallogr., Sect. D: Struct. Biol.* **74**, 1129–1168 (2018).
- ³⁵P. Luo, A. Jaiswal, Y. Zhai, Z. Cai, N. P. Walter, L. Zhou, D. Ding, M. Liu, R. Mills, A. Podlesnyak, G. Ehlers, A. Faraone, H. Bai, W. Wang, and Y. Z., "Atomic dynamics of metallic glass melts $\text{La}_{50}\text{Ni}_{15}\text{Al}_{35}$ and $\text{Ce}_{70}\text{Cu}_{19}\text{Al}_{11}$ studied by quasielastic neutron scattering," *Phys. Rev. B* **103**, 224104 (2021).
- ³⁶A. Jaiswal, T. Egami, K. F. Kelton, K. S. Schweizer, and Y. Zhang, "Correlation between fragility and the Arrhenius crossover phenomenon in metallic, molecular, and network liquids," *Phys. Rev. Lett.* **117**, 205701 (2016).
- ³⁷A. Jaiswal, A. Podlesnyak, G. Ehlers, R. Mills, S. O'Keeffe, J. Stevick, J. Kempton, G. Jelbert, W. Dmowski, K. Lokshin, T. Egami, and Y. Zhang, "Coincidence of collective relaxation anomaly and specific heat peak in a bulk metallic glass-forming liquid," *Phys. Rev. B* **92**, 024202 (2015).
- ³⁸A. Jaiswal, S. O'Keeffe, R. Mills, A. Podlesnyak, G. Ehlers, W. Dmowski, K. Lokshin, J. Stevick, T. Egami, and Y. Zhang, "Onset of cooperative dynamics in an equilibrium glass-forming metallic liquid," *J. Phys. Chem. B* **120**(6), 1142–1148 (2016).
- ³⁹R. Ashcraft, Z. Wang, D. L. Abernathy, D. G. Quirinale, T. Egami, and K. F. Kelton, "Experimental determination of the temperature-dependent Van Hove function in a $\text{Zr}_{80}\text{Pt}_{20}$ liquid," *J. Chem. Phys.* **152**(7), 074506 (2020).
- ⁴⁰T. Albrecht, C. Bührer, M. Fähnle, K. Maier, D. Platzek, and J. Reske, "First observation of ferromagnetism and ferromagnetic domains in a liquid metal," *Appl. Phys. A* **65**, 215–220 (1997).
- ⁴¹J. Reske, D. M. Herlach, F. Keuser, K. Maier, and D. Platzek, "Evidence for the existence of long-range magnetic ordering in a liquid undercooled metal," *Phys. Rev. Lett.* **75**, 737–739 (1995).
- ⁴²W. Doster, S. Cusack, and W. Petry, "Dynamical transition of myoglobin revealed by inelastic neutron scattering," *Nature* **337**, 754–756 (1989).
- ⁴³B. Frick and D. Richter, "The microscopic basis of the glass transition in polymers from neutron scattering studies," *Science* **267**(5206), 1939–1945 (1995).
- ⁴⁴P. Luo, Y. Zhai, E. Senses, E. Mamontov, G. Xu, Y. Z., and A. Faraone, "Influence of kosmotrope and chaotrope salts on water structural relaxation," *J. Phys. Chem. Lett.* **11**, 8970–8975 (2020).
- ⁴⁵K. Yang, Z. Cai, A. Jaiswal, M. Tyagi, J. S. Moore, and Y. Zhang, "Dynamic odd-even effect in liquid *n*-alkanes near their melting points," *Angew. Chem., Int. Ed.* **55**(45), 14090–14095 (2016).
- ⁴⁶N. P. Walter, A. Jaiswal, Z. Cai, and Y. Zhang, "LiquidLib: A comprehensive toolbox for analyzing classical and *ab initio* molecular dynamics simulations of liquids and liquid-like matter with applications to neutron scattering experiments," *Comput. Phys. Commun.* **228**, 209–218 (2018).
- ⁴⁷D. L. Abernathy, J. L. Niedziela, and M. B. Stone, "Extracting source parameters from beam monitors on a chopper spectrometer," *EPJ Web Conf.* **83**, 03001 (2015).
- ⁴⁸J. M. Carpenter, D. L. Price, and N. J. Swanson, "IPNS—A national facility for condensed matter research," Report No. ANL 78-88, 1978, p. 291.
- ⁴⁹G. Shirane, S. M. Shapiro, and J. M. Tranquada, *Neutron Scattering with a Triple-Axis Spectrometer: Basic Techniques* (Cambridge University Press, 2002).
- ⁵⁰G. Ehlers, G. Sala, F. Gallmeier, and K. W. Herwig, "Figure-of-merit for a cold coupled moderator at the SNS second target station suited for direct geometry inelastic spectrometers," *J. Phys.: Conf. Ser.* **1021**, 012032 (2018).
- ⁵¹F. X. Gallmeier, W. Lu, B. W. Riemer, J. K. Zhao, K. W. Herwig, and J. L. Robertson, "Conceptual moderator studies for the Spallation Neutron Source short-pulse second target station," *Rev. Sci. Instrum.* **87**(6), 063304 (2016).
- ⁵²G. Ehlers, A. A. Podlesnyak, J. L. Niedziela, E. B. Iverson, and P. E. Sokol, "The new cold neutron chopper spectrometer at the spallation neutron source: Design and performance," *Rev. Sci. Instrum.* **82**(8), 085108 (2011).
- ⁵³R. I. Bewley, J. W. Taylor, and S. M. Bennington, "LET, a cold neutron multi-disk chopper spectrometer at ISIS," *Nucl. Instrum. Methods Phys. Res., Sect. A* **637**(1), 128–134 (2011).
- ⁵⁴K. Nakajima, S. Ohira-Kawamura, T. Kikuchi, M. Nakamura, R. Kajimoto, Y. Inamura, N. Takahashi, K. Aizawa, K. Suzuya, K. Shibata, T. Nakatani, K. Soyama, R. Maruyama, H. Tanaka, W. Kambara, T. Iwahashi, Y. Itoh, T. Osakabe, S. Wakimoto, K. Kakurai, F. Maekawa, M. Harada, K. Oikawa, R. E. Lechner, F. Mezei, and M. Arai, "AMATERAS: A cold-neutron disk chopper spectrometer," *J. Phys. Soc. Jpn.* **80**(Suppl.B), SB028 (2011).
- ⁵⁵K. Lefmann, K. Nielsen, A. Tennant, and B. Lake, "McStas 1.1: A tool for building neutron Monte Carlo simulations," *Physica B* **276–278**, 152–153 (2000).
- ⁵⁶J. Y. Y. Lin, H. L. Smith, G. E. Granroth, D. L. Abernathy, M. D. Lumsden, B. Winn, A. A. Aczel, M. Aivazis, and B. Fultz, "MCVINE—An object oriented Monte Carlo neutron ray tracing simulation package," *Nucl. Instrum. Methods Phys. Res., Sect. A* **810**, 86–99 (2016).
- ⁵⁷J. Y. Y. Lin, F. Islam, G. Sala, I. Lumsden, H. Smith, M. Doucet, M. B. Stone, D. L. Abernathy, G. Ehlers, J. F. Ankner, and G. E. Granroth, "Recent developments of MCVINE and its applications at SNS," *J. Phys. Commun.* **3**, 085005 (2019).
- ⁵⁸O. Arnold, J. C. Bilheux, J. M. Borreguero, A. Buts, S. I. Campbell, L. Chapon, M. Doucet, N. Draper, R. Ferraz Leal, M. A. Gigg, V. E. Lynch, A. Markvardsen, D. J. Mikkelsen, R. L. Mikkelsen, R. Miller, K. Palmen, P. Parker, G. Passos, T. G. Perring, P. F. Peterson, S. Ren, M. A. Reuter, A. T. Savici, J. W. Taylor, R. J. Taylor, R. Tolchenov, W. Zhou, and J. Zikovsky, "Mantid—Data analysis and visualization package for neutron scattering and μ SR experiments," *Nucl. Instrum. Methods Phys. Res., Sect. A* **764**, 156–166 (2014).
- ⁵⁹S. Itoh, K. Ueno, R. Ohkubo, H. Sagehashi, Y. Funahashi, and T. Yokoo, "T0 chopper developed at KEK," *Nucl. Instrum. Methods Phys. Res., Sect. A* **661**(1), 86–92 (2012).
- ⁶⁰G. E. Granroth, A. I. Kolesnikov, T. E. Sherline, J. P. Clancy, K. A. Ross, J. P. C. Ruff, B. D. Gaulin, and S. E. Nagler, "SEQUOIA: A newly operating chopper spectrometer at the SNS," *J. Phys.: Conf. Ser.* **251**, 012058 (2010).
- ⁶¹D. L. Abernathy, M. B. Stone, M. J. Loguillo, M. S. Lucas, O. Delaire, X. Tang, J. Y. Y. Lin, and B. Fultz, "Design and operation of the wide angular-range chopper spectrometer ARCS at the spallation neutron source," *Rev. Sci. Instrum.* **83**(1), 015114 (2012).

- ⁶²R. I. Bewley, J. W. Taylor, and S. M. Bennington, "LET: A low energy multiple chopper spectrometer at ISIS," *Not. Neutroni Luce Sincrotrone* **16**(2), 4–13 (2011).
- ⁶³T. Kikuchi, K. Nakajima, S. Ohira-Kawamura, Y. Inamura, M. Nakamura, D. Wakai, K. Aoyama, T. Iwahashi, and W. Kambara, "Background issues encountered by cold-neutron chopper spectrometer AMATERAS," *Physica B* **564**, 45, 7–53 (2019).
- ⁶⁴M. B. Stone, J. L. Niedziela, D. L. Abernathy, L. DeBeer-Schmitt, G. Ehlers, O. Garlea, G. E. Granroth, M. Graves-Brook, A. I. Kolesnikov, A. Podlesnyak, and B. Winn, "A comparison of four direct geometry time-of-flight spectrometers at the spallation neutron source," *Rev. Sci. Instrum.* **85**(4), 045113 (2014).
- ⁶⁵M. B. Stone, L. Crow, V. R. Fanelli, and J. L. Niedziela, "Characterization of shielding materials used in neutron scattering instrumentation," *Nucl. Instrum. Methods Phys. Res., Sect. A* **946**, 162708 (2019).
- ⁶⁶N. A. Mauro, A. J. Vogt, K. S. Derendorf, M. L. Johnson, G. E. Rustan, D. G. Quirinale, A. Kreyssig, K. A. Lokshin, J. C. Neufeind, K. An, X.-L. Wang, A. I. Goldman, T. Egami, and K. F. Kelton, "Electrostatic levitation facility optimized for neutron diffraction studies of high temperature liquids at a spallation neutron source," *Rev. Sci. Instrum.* **87**(1), 013904 (2016).
- ⁶⁷G. Sala, J. Y. Y. Lin, V. B. Graves, and G. Ehlers, "Conceptual design of CHES, a new direct-geometry inelastic neutron spectrometer dedicated to studying small samples," *J. Appl. Crystallogr.* **51**, 282–293 (2018).
- ⁶⁸V. F. Sears, *Neutron Optics* (Oxford University Press, 1989).
- ⁶⁹R. Kajimoto, M. Nakamura, T. Osakabe, T. J. Sato, K. Nakajima, and M. Arai, "Study of converging neutron guides for the cold neutron double-chopper spectrometer at J-PARC," *Physica B* **385–386**, 1236–1239 (2006).
- ⁷⁰K. H. Kleno, K. Lieutenant, K. H. Andersen, and K. Lefmann, "Systematic performance study of common neutron guide geometries," *Nucl. Instrum. Methods Phys. Res., Sect. A* **696**, 75–84 (2012).
- ⁷¹P. M. Bentley, S. J. Kennedy, K. H. Andersen, D. Martin Rodríguez, and D. F. R. Mildner, "Correction of optical aberrations in elliptic neutron guides," *Nucl. Instrum. Methods Phys. Res., Sect. A* **693**, 268, 11–275 (2012).
- ⁷²C. Zender, D. Nekrassov, and K. Lieutenant, "An improved elliptic guide concept for a homogeneous neutron beam without direct line of sight," *Nucl. Instrum. Methods Phys. Res., Sect. A* **746**, 39–46 (2014).
- ⁷³P. Willendrup, E. Farhi, E. Knudsen, U. Filges, and K. Lefmann, "McStas: Past, present and future," *J. Neutron Res.* **17**(1), 35–43 (2014).
- ⁷⁴P. K. Willendrup and K. Lefmann, "McStas (i): Introduction, use, and basic principles for ray-tracing simulations," *J. Neutron Res.* **22**, 1–16 (2020).
- ⁷⁵P. K. Willendrup and K. Lefmann, "McStas (ii): An overview of components, their use, and advice for user contributions," *J. Neutron Res.* **23**(1), 7–27 (2021).
- ⁷⁶J. C. E. A. Hafner, T. Kluyver, M. Bertelsen, M. U. Kahaly, Z. Lecz, S. Nourbakhsh, A. P. Mancuso, and C. Fortmann-Grote, "VINYL: The Virtual neutron and x-ray laboratory and its applications," *Proc. SPIE* **11493**, 114930Z (2020).
- ⁷⁷See <https://github.com/panosc-vinyl/mcstascript> for information related to the software and technical details.
- ⁷⁸M. Newville, T. Stensitzki, D. B. Allen, and A. Ingarciola (2014). "LMFIT: Non-linear least-square minimization and curve-fitting for Python," Zenodo, V. 0.8.0, <https://doi.org/10.5281/zenodo.11813>.
- ⁷⁹A. Houben, W. Schweika, T. Brückel, and R. Dronskowski, "New neutron-guide concepts and simulation results for the POWTEX instrument," *Nucl. Instrum. Methods Phys. Res., Sect. A* **680**, 124–133 (2012).
- ⁸⁰J. Voigt, N. Violini, and T. Brückel, "Chopper layout for spectrometers at long pulse neutron sources," *Nucl. Instrum. Methods Phys. Res., Sect. A* **741**, 26–32 (2014).
- ⁸¹A. Vickery and P. P. Deen, "Choppers to optimise the repetition rate multiplication technique on a direct geometry neutron chopper spectrometer," *Rev. Sci. Instrum.* **85**(11), 115103 (2014).
- ⁸²P. P. Deen, A. Vickery, K. H. Andersen, and R. Hall-Wilton, "A design study of VOR: A versatile optimal resolution chopper spectrometer for the ESS," *EPJ Web Conf.* **83**, 03002 (2015).
- ⁸³K. H. Andersen, M. Bertelsen, L. Zanini, E. B. Klinkby, T. Schönfeldt, P. M. Bentley, and J. Saroun, "Optimization of moderators and beam extraction at the ESS," *J. Appl. Crystallogr.* **51**, 264–281 (2018).
- ⁸⁴S. Ohira-Kawamura, R. Takahashi, M. Ishikado, Y. Yamauchi, M. Nakamura, K. Ohuchi, H. Kira, W. Kambara, K. Aoyama, Y. Sakaguchi, M. Watanabe, and T. Oku, "Cryogenic sample environments shared at the MLF, J-PARC," *J. Neutron Res.* **21**(1–2), 17–22 (2019).
- ⁸⁵K. Nakajima, S. Ohira-Kawamura, M. Kofu, N. Murai, Y. Inamura, T. Kikuchi, and D. Wakai, "Recent update of AMATERAS: A cold-neutron disk-chopper spectrometer," *JPS Conf. Proc.* **33**, 011089 (2021).
- ⁸⁶M. B. Stone, D. H. Siddel, A. M. Elliott, D. Anderson, and D. L. Abernathy, "Characterization of plastic and boron carbide additive manufactured neutron collimators," *Rev. Sci. Instrum.* **88**(12), 123102 (2017).
- ⁸⁷M. B. Stone, G. Sala, and J. Y. Y. Lin, "Design of a radial collimator for the SEQUOIA direct geometry chopper spectrometer," *Physica B* **564**, 17–21 (2019).
- ⁸⁸F. Islam, J. Lin, T. Huegle, I. Lumsden, D. Anderson, A. Elliott, B. Haberl, and G. Granroth, "Computational optimization of a 3D printed collimator," *J. Neutron Res.* **22**(2–3), 155–168 (2020).
- ⁸⁹F. F. Islam, B. Haberl, J. Y. Y. Lin, D. C. Anderson, J. J. Molaison, and G. E. Granroth, "Novel data analysis method for obtaining better performance from a complex 3D-printed collimator," *Nucl. Instrum. Methods Phys. Res., Sect. A* **1014**, 165646 (2021).
- ⁹⁰C. L. Cramer, A. M. Elliott, J. O. Kiggans, B. Haberl, and D. C. Anderson, "Processing of complex-shaped collimators made via binder jet additive manufacturing of B₄C and pressureless melt infiltration of Al," *Mater. Des.* **180**, 107956 (2019).
- ⁹¹B. Haberl, J. J. Molaison, M. Frontzek, E. C. Novak, G. E. Granroth, D. Goldsby, D. C. Anderson, and A. M. Elliott, "3D-printed B₄C collimation for neutron pressure cells," *Rev. Sci. Instrum.* **92**(9), 093903 (2021).
- ⁹²See <https://www.tanerxun.com/mechanical-iris-shutter-mechanism/html> for information on the technical specifications of the mechanism.
- ⁹³N. Violini, J. Voigt, S. Pasini, and T. Brückel, "A method to compute the covariance matrix of wavevector-energy transfer for neutron time-of-flight spectrometers," *Nucl. Instrum. Methods Phys. Res., Sect. A* **736**, 31–39 (2014).
- ⁹⁴L. Abuel, F. Bartsch, A. Berry, J. C. Buffet, S. Cuccaro, P. van Esch, B. von Guérard, S. Holt, J. Marchal, P. Mutti, K. Ollivier, J. Pentenero, M. Platz, A. Robert, D. Roulier, and J. L. Spedding, "First measurements with the new ³He-filled monoblock aluminium multitube neutron detector developed at the ILL for ANSTO PLATYPUS reflectometer," *J. Neutron Res.* **23**, 53 (2021).
- ⁹⁵A. Khaplanov, F. Piscitelli, J.-C. Buffet, J.-F. Clergeau, J. Correa, P. van Esch, M. Ferraton, B. Guerard, and R. Hall-Wilton, "Investigation of gamma-ray sensitivity of neutron detectors based on thin converter films," *J. Instrum.* **8**, P10025 (2013).
- ⁹⁶G. Mauri, F. Messi, K. Kanaki, R. Hall-Wilton, and F. Piscitelli, "Fast neutron sensitivity for ³He detectors and comparison with Boron-10 based neutron detectors," *EPJ Tech. Instrum.* **6**, 3 (2019).
- ⁹⁷M. Anastasopoulos, R. Bebb, K. Berry, J. Birch, T. Brys, J.-C. Buffet, J.-F. Clergeau, P. P. Deen, G. Ehlers, P. van Esch, S. M. Everett, B. Guerard, R. Hall-Wilton, K. Herwig, L. Hultman, C. Höglund, I. Iruretagoiena, F. Issa, J. Jensen, A. Khaplanov, O. Kirstein, I. L. Higuera, F. Piscitelli, L. Robinson, S. Schmidt, and I. Stefanescu, "Multi-grid detector for neutron spectroscopy: Results obtained on time-of-flight spectrometer CNCS," *J. Instrum.* **12**, P04030 (2017).
- ⁹⁸F. Issa, A. Khaplanov, R. Hall-Wilton, I. Llamas, M. D. Riktor, S. R. Brattheim, and H. Perrey, "Characterization of thermal neutron beam monitors," *Phys. Rev. Accel. Beams* **20**, 092801 (2017).
- ⁹⁹I. I. Al-Qasir, A. A. Campbell, G. Sala, J. Y. Y. Lin, Y. Cheng, F. F. Islam, D. L. Abernathy, and M. B. Stone, "Vacancy-driven variations in the phonon density of states of fast neutron irradiated nuclear graphite," *Carbon* **168**, 42–54 (2020).
- ¹⁰⁰J. Y. Y. Lin, G. Sala, and M. B. Stone, "A super-resolution technique to analyze single-crystal inelastic neutron scattering measurements using direct-geometry chopper spectrometers," *Rev. Sci. Instrum.* **93**(2), 025101 (2022).
- ¹⁰¹M. D. Lumsden, S. E. Nagler, B. C. Sales, D. A. Tennant, D. F. McMorrow, S.-H. Lee, and S. Park, "Magnetic excitation spectrum of the square

lattice $S = 1/2$ Heisenberg antiferromagnet $K_2V_3O_8$,” *Phys. Rev. B* **74**, 214424 (2006).

¹⁰²L. Robertson and T. Huegle, personal communications (2019).

¹⁰³J. R. D. Copley, “Optimized design of the chopper disks and the neutron guide in a disk chopper neutron time-of-flight spectrometer,” *Nucl. Instrum. Methods Phys. Res., Sect. A* **291**, 519–532 (1990).

¹⁰⁴J. R. D. Copley, “Transmission properties of a counter-rotating pair of disk choppers,” *Nucl. Instrum. Methods Phys. Res., Sect. A* **303**, 332–341 (1991).

¹⁰⁵J. R. D. Copley, “An acceptance diagram analysis of the contaminant pulse removal problem with direct geometry neutron chopper spectrometers,” *Nucl. Instrum. Methods Phys. Res., Sect. A* **510**, 318–324 (2003).